



HAL
open science

An educational review on distributed optic fiber sensing based on Rayleigh backscattering for damage tracking and structural health monitoring

Ludovic Chamoin, S Farahbakhsh, M Poncelet

► To cite this version:

Ludovic Chamoin, S Farahbakhsh, M Poncelet. An educational review on distributed optic fiber sensing based on Rayleigh backscattering for damage tracking and structural health monitoring. Measurement Science and Technology, 2022, 33, pp.124008. 10.1088/1361-6501/ac9152 . hal-03701630v2

HAL Id: hal-03701630

<https://hal.science/hal-03701630v2>

Submitted on 17 Oct 2022

HAL is a multi-disciplinary open access archive for the deposit and dissemination of scientific research documents, whether they are published or not. The documents may come from teaching and research institutions in France or abroad, or from public or private research centers.

L'archive ouverte pluridisciplinaire **HAL**, est destinée au dépôt et à la diffusion de documents scientifiques de niveau recherche, publiés ou non, émanant des établissements d'enseignement et de recherche français ou étrangers, des laboratoires publics ou privés.

Review Article

An educational review on distributed optic fiber sensing based on Rayleigh backscattering for damage tracking and structural health monitoring

L Chamoin^{1,2}, S Farahbakhsh¹ and M Poncelet¹

¹ Université Paris-Saclay, CentraleSupélec, ENS Paris-Saclay, CNRS, LMPS-Laboratoire de Mécanique Paris-Saclay, 91190 Gif-sur-Yvette, France

² Institut Universitaire de France (IUF), 1 rue Descartes, 75005 Paris, France

E-mail: ludovic.chamoin@ens-paris-saclay.fr,
sahar.farahbakhsh@ens-paris-saclay.fr,
martin.poncelet@ens-paris-saclay.fr

August 2022

Abstract. This paper is a review on distributed optic fiber sensing for structural health monitoring applications, with a deeper focus on technologies relying on the Rayleigh backscattering phenomenon. It addresses the basic physical principles which are involved, the implementation and instrumentation of the measurement techniques, as well as recent practical applications, current performance, and remaining challenges. Being written at an elementary level and integrating relevant theoretical and technical details, we hope the document can be useful for researchers and engineers looking for an up-to-date overview on a field which currently undergoes significant development and increasing attractiveness, in particular for damage tracking in complex mechanical structures.

Keywords: Structural health monitoring, Optic fiber sensing, Rayleigh backscattering, Structural mechanics

Submitted to: *Meas. Sci. Technol.*

1. Introduction

Damage phenomena in mechanical structures have always been a perpetual engineering issue, for the sake of durability and safety. Initiated locally and at small scale from manufacturing defects, impacts, excessive loading, or other unexpected events, such complex nonlinear phenomena may be precursors of an overall structural performance decrease (e.g. through ageing or fatigue processes) which may lead to dramatic consequences. It is thus of paramount importance to make diagnosis, from an early stage of

development, on the internal damage state of critical mechanical structures employed in various activities, e.g. energy or transport (aircrafts, bridges, wind turbines. . .), and control damage growth along the structure life. This is the goal of Structural Health Monitoring (SHM) [220, 72] which is both an active research topic and a major industrial challenge [39]. Nowadays, and out of well-trained (but still subjective and limited) engineering visual inspection, effective damage tracking on large engineering structures is made possible with cutting edge developments of non-destructive sensing techniques, that permit to inform on the internal material state with high accuracy and spatial resolution [143, 232]. These are progressively replacing traditional point sensors e.g. strain gauges or displacement transducers as they provide much richer experimental information, e.g. with full-field measurements. Among these advanced and powerful sensing techniques, we may list image-based approaches e.g. Digital Image Correlation (DIC) or Digital Volume Correlation (DVC) [162, 107, 201, 238], acoustic emission e.g. through Lamb waves [202], vibration-based sensing [60, 69, 43], or embedded micro-sensor arrays [207, 12] using electrically conductive carbon nanotubes [229, 46, 91, 102, 254] or optic fibers [258, 82, 50, 234].

The rich sensing information which is now available can be used to feed and complement elaborated multiscale computational damage models, that may be physics-based (inheriting from a rich history of engineering sciences and computational mechanics) and/or data-driven i.e. defined from clustering and learning algorithms [193, 70, 122, 230, 11, 200]. The link between sensor data and modeling, in terms of digital or hybrid twins [45], permits to better interpret data in damage diagnosis, to assess the structural behavior e.g. through inverse analysis and parameter identification [48, 47, 228, 247, 76, 244, 147, 185], to perform effective simulation-based prediction by exploiting all available knowledge, and eventually to take anticipated actions to guaranty the structural integrity. This trend is emphasized and pushed forward in a recent methodology, referring to the Dynamic Data-Driven Application Systems (DDDAS) paradigm [53, 54]. It aims at continuously and synergistically connecting advanced in-situ sensing devices with high-fidelity simulation tools for on-the-fly data assimilation, real-time damage diagnosis and prognosis, and safe decision-making with appropriate in-service adaptation of the operating plan e.g. with continuous load monitoring, in order to meet preset objectives. Provided some effective numerical algorithms are also implemented on dedicated portable computing platforms involving GPUs or FPGAs, this process would permit online continuous supervision and control of complex damage phenomena on a structure during service before downtime or failure occur. Such a multidisciplinary methodology thus represents a key enabler for the next generation of on-board SHM technologies, envisioning the design of smart autonomous mechanical structures with integrated SHM capabilities, enhanced damage tolerance, timely optimized (reduced and condition-based) maintenance, capability to operate in degraded mode so that the operational life cycle is extended and better coherence with sustainable protecting policies is reached, and thus increased reliability and performance [41].

In this paper, we specifically deal with advanced sensing techniques based on the use of optic fibers [233, 75, 82, 50, 90], which have been the topic of many research studies and regular improvements. They have experienced a fast economic growth over the last decade with a market growing at a compound annual growth rate of 15% these last years [156], and are becoming more and more popular for in-situ SHM applications in various engineering fields such as civil engineering, geotechnics, aeronautics, or manufacturing (see [37, 112, 150, 92, 165, 106, 139, 188, 249, 56, 194, 25, 187, 208, 148, 219, 103, 15] to cite a few). Out of telecommunication [100, 1, 101], standard optic fibers indeed have a widespread use as sensing elements (both transducer and transmitter) in order to remotely measure, from scattering physical phenomena, the mechanical strain but also temperature or other physical quantities potentially, e.g. magnetic field or humidity, inside complex materials such as concrete or laminate composites. Damage phenomena, in terms of local change in material properties that degrades structural performance, can then be recovered from updated strain information. When associated with distributed measurement, i.e. simultaneous continuous-in-space measurement along the sensing fiber under test (FUT), this refers to Distributed Optical Fiber Sensors (DOFS) from which 1D full-field measurements with zero-dead zone are made and analyzed [199]. The procedure implies using a connected and active optoelectronic monitoring unit (interrogator) that sends light into the fiber then collects and processes, with dedicated software, the returned signal to retrieve the desired measurement information from signal features. Distributed optical fiber sensors, characterized by spatially resolved measurements along a continuous fiber, represent the highest state-of-the-art in optical sensing. Let us also mention discrete multi-point optic fiber sensors, such as those based on Fiber Bragg Gratings (FBGs) [108], which are widely used for SHM [231, 22, 155, 184, 8, 55, 177, 215, 124, 64].

In addition to unique measurement capabilities in terms of sensing distance and density, being such that a single fiber may replace a large amount of conventional sensors, many other inherent advantages of DOFS technologies compared to alternative sensing technologies may be listed [149, 96]:

- flexibility in installation and use, with easiness to bond to and even embed into the structure, low-intrusiveness due to small size, lightweight for transport/handling/portability with no bulky sensing equipment, low price of the fiber sensing elements (compared to strain gauges for instance), no need for electrical energy supply or connection along the electrically passive measurement line, and remote in-situ sensing with possible multiplexing, e.g. by using several measurement channels with a single interrogator. This has to be compared with many alternative sensing technologies, such as external optical measurements or acoustic emission, which are difficult to use out of the lab;
- large range of applications, with capability to get measurements and be durable in harsh (radiative, corrosive) environments [29], to be stable and reliable with high chemical or thermal effects, to cover large measurement zones, to scan with high

rate (up to 100-1000 Hz) so that the continuous capture of phenomena ranging from operational deformations to impact damage is possible, and immunity of the signal to electromagnetic interference (EMI). This has to be compared with many alternative sensing technologies which require repetitive calibration and do not offer reliable long-term measurements due to drifting by aging, or those which do not permit real-time measurement due to long post-processing requirements.

Optic fiber sensors thus constitute a very promising area for enhancing the accuracy and effectiveness of damage detection in SHM practices. Nevertheless, they also go with some drawbacks which will be addressed hereafter; we may list the care required to install the sensing technology due to the fragility of the fiber, the difficulty to embed the fiber in very small structures due to its non-negligible size, or the relatively high cost (potentially > 150 k€) of the interrogation unit.

A large literature exists on optic fiber technologies as powerful sensing devices, based on the various scattering mechanisms (Raman, Brillouin, Rayleigh...) concurrently occurring inside fibers, each presenting advantages and limitations depending on the objectives and specificity of the monitoring solution. Early developments can be found in [126, 198], and the interested reader may refer to [4, 84, 86, 234, 18, 71, 153] for an overview. We also mention that some optic fiber sensing technologies, referring to interferometric sensors e.g. Fabry-Perot sensors, Mach-Zehnder sensors, Sagnac sensors [49, 138], are based on the change of the optical phase generated by varying physical quantities such as angular speed in gyroscopes [132, 251]; as these technologies permit single-point detection only, and have a low multiplexing capability and limited dynamic measurement range, they will not be addressed here.

In the present paper, and even though we review the main DOFS technologies, we specifically focus on some taking advantage of the Rayleigh backscattering [77, 206, 176]. These are nowadays very attractive as they can deliver real-time distributed characterization of the strain field (static and dynamic) with unmatched spatial resolution (thousands of measurements per meter). They are thus a good candidate for the online detection of localized unexpected events as damage. Such technologies have already been employed in several applications and are increasingly envisioned by industrialists for integrated SHM [56]. With this review paper, the wish is to provide a comprehensive vision on these. We thus first present physical phenomena and sensing methodologies associated with Rayleigh backscattering, from an educational perspective, before giving details on the technological implementation and illustrating the potential with recent applications.

The paper is organized as follows: after this introduction, basic general information on optic fiber sensing with associated optical properties and physical phenomena is provided in Section 2; a deeper focus on sensing principles and technologies relying on Rayleigh backscattering is made in Section 3; recent applications and research advances on these latter technologies, as well as challenges, are reported in Section 4; concluding remarks are eventually given in Section 5.

2. Basics on sensing with optic fibers

2.1. Waveguide properties of optic fibers

The typical geometry of a standard optic fiber, used for both telecom and sensing applications, is given in Figure 1. It is a cylindric piece, with length far larger than diameter, that includes three parts:

- a core, in which light propagates. Its size is about 5-10 μm in diameter (i.e. a few injected light wavelengths) for single-mode fibers (SMF), while it may reach 50-80 μm in diameter for multi-mode fibers (MMF);
- a cladding (optical sleeve), surrounding the core. Its size is in the order of 125 μm in diameter;
- a coating (protection sleeve), surrounding the cladding. It protects the fiber against environmental impacts and increases its mechanical resistance. This additional layer usually takes the fiber to a total diameter of 150-250 μm similar to a human hair, even though it may reach a few millimeters for specific applications such as sensing in concrete materials, when an additional thicker protection is used. The coating is usually made of plastic material, that is acrylate or polyamide depending on the temperature of use. Given the application, its internal surface may be bonded to the cladding (e.g. for strain sensing), or detached from it to be insensitive to physical deformations (e.g. for temperature sensing).

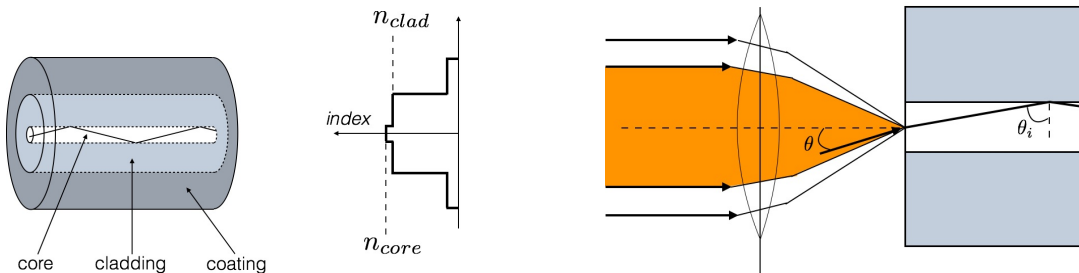


Figure 1. Geometry of a step-index optic fiber (left), with total internal reflection in the core and numerical aperture of the obtained waveguide (right).

The core and cladding are made of a very transparent and stable silica glass (SiO_2) compound. Pure silica is used for the cladding, with constant index $n_{clad} \sim 1.46$, while silica in the core is suitably doped (typically using Germanium or Phosphorus [120]) in order to increase the index up to a value $n_{core} > n_{clad}$, with $\Delta n/n_{clad}$ from a few 10^{-3} (SMF fibers) to 10^{-2} (MMF fibers). This increase may be constant (step-index fiber) or not (gradient-index fiber) in the core section. The core and cladding are in practice simultaneously manufactured by pulling out the same glass preform, which is a much shorter and thicker rod. Typically, a preform with initial length 1 m and diameter 5 cm will produce a fiber with length 160 km and diameter 125 μm . The preform is then

doped during the process, in order to obtain an index profile which is about homothetic of that of the final fiber.

Basic propagation principles inside optic fibers can be understood from geometrical optics. When light is injected in the core, from either a broadband source or a narrow linewidth laser, and due to the slightly higher refractive index of the core, total internal reflection at the core-cladding interface is possible. This requires that the incident angle θ_i at the interface be larger than a critical angle θ_c defined from the Snell-Descartes law as $\theta_c = \arcsin(n_{clad}/n_{core})$. As the fiber is excited from the lateral side through rays travelling in a medium with refractive index $n_0 \sim 1$, the input incident angle θ of the rays should be smaller than an acceptance angle θ_0 called *numerical aperture* and given by:

$$\theta_0 \approx \sin \theta_0 = n_{core} \sin\left(\frac{\pi}{2} - \theta_c\right) = \sqrt{n_{core}^2 - n_{clad}^2} \approx \sqrt{2n_{core}\Delta n} \quad (\Delta n \ll 1) \quad (2.1)$$

It defines an acceptance cone around the fiber axis (see Figure 1). Typical values of θ_0 vary between 0.11 rad (6°) for SMF fibers and 0.17 rad (10°) for MMF fibers.

When total reflexion occurs, it confines the light energy inside a restricted volume and the fiber behaves as a dielectric waveguide with propagation along its axis [218, 101, 35]. Useful information on waveguide properties and features is recalled in Appendix A, where a complementary wave-based description of propagation is used for better interpretation. Waveguide propagation provides a finite set of discrete solutions which correspond to allowed guided optic modes, each defined by a value of the incident angle of light rays, a specific transverse distribution of electric/magnetic fields, and an effective refractive index $n_{eff} \in [n_{clad}, n_{core}[$ with associated longitudinal speed c_0/n_{eff} (phase velocity) at a given input wavelength or frequency. The effective propagating region of the core and cladding glass is known as the mode field.

Waveguide properties fully depend on features of the injected signal (wavelength λ_0) and design parameters of the fiber (refractive index profile, core diameter). SMF fibers, preferred for long transmission length and/or high debits, admit the propagation of a single guided mode (fundamental mode) with rays at grazing incidence. For some applications with short distance communications, MMF fibers with larger core diameter and input power are used that allow the propagation of several waveguide modes with intermodal dispersion. The limit for mode acceptance is reached when the conditions for total reflection are no longer satisfied.

A key parameter is the dimensionless normalized (or reduced) frequency:

$$V = k_0 a \sqrt{n_{core}^2 - n_{clad}^2} \quad (2.2)$$

with $k_0 = 2\pi/\lambda_0$ the wavenumber of the input light beam (in the air or vacuum) and a the core radius. The parameter V determines the monomodal/multimodal feature of the fiber as well as the number of admitted guided modes for a given frequency (see Appendix A). If $V < 2.405$, which corresponds to the first zero of the Bessel function that appears in guided solutions, the optic fiber is single-mode; otherwise, it is multimode

and the number M of modes that the fiber can support is $M = 4V^2/\pi^2$ asymptotically (i.e. when $V \gg 1$) for a step-index fiber. The specific cut-off wavelength associated with the propagation of a second mode is around 1,260 nm for classical fibers, which operate between 1,300 nm and 1,600 nm for SMF, and around 850 nm for MMF.

2.2. Optical loss and scattering phenomena

Some major aspects of propagation in optic fibers are optical distortion (flattening) of the original light signal, due to chromatic guide dispersion, and attenuations i.e. losses in optic power along the propagation. Such attenuations may be partly due to index mismatch, in terms of Fresnel peaks producing reflection, at connections with glass-to-air transitions or dielectric interfaces, to environmental conditions such as irradiation, to excessive fiber curvature, or to micro-bending [181]. Nevertheless, even though silica is chosen as it has very low optical loss, some other sources of attenuation along the fiber are intrinsic to the material i.e. are generated by interactions between light and the propagating medium, and may become significant for long propagation distances. Attenuation can then be described as (Beer-Lambert's law):

$$P(\lambda, z) = P_0 \cdot 10^{-\alpha(\lambda)z} = P_0 \cdot 10^{-\alpha_{dB}(\lambda)z/10} \quad (2.3)$$

with P_0 (resp. $P(\lambda, z)$) the optic power at the entrance (resp. at position z in km) of the fiber, and α (resp. α_{dB}) the fiber lineic attenuation coefficient in km^{-1} (resp. dB.km^{-1}) which depends on the wavelength λ of the propagating signal.

The low attenuation window is limited in the short wavelength region (below 300 nm) by ultraviolet absorption with electronic origin, and in the long wavelength region (above 2 μm) by infrared multi-phonon absorption with SiO_2 molecular dipole origin. Within these limits the material can be considered transparent. The attenuation diagram of silica glass in the overall wavelength range is shown in Figure 2; it indicates that silica fibers have a minimal attenuation around 1,550 nm (near infrared) which is then the input wavelength usually favored for SMF fibers. For such a wavelength, progress in manufacturing nowadays enables to reach a natural loss of 0.2 dB.km^{-1} for standard SMF fibers, meaning that 1% of the injected signal power remains after 100 km of propagation. This low value is to be compared to the 100 dB.km^{-1} attenuation of the best coaxial radio and microwave cables.

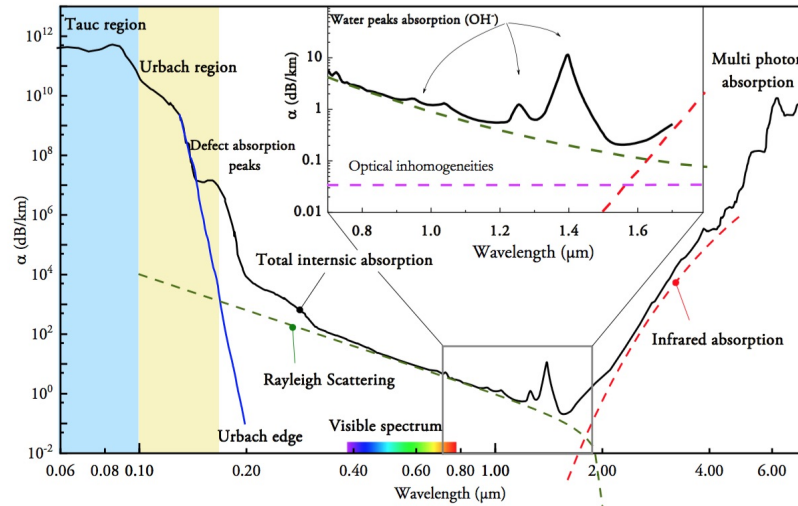


Figure 2. Attenuation with respect to wavelength in a typical silica optic fiber (from [38]).

In the low-attenuation regime, a dominant intrinsic loss source is Rayleigh scattering for which intensity evolves in λ^{-4} due to its electric dipolar origin [250, 170, 94, 173, 2, 204]; it thus limits guiding performance for short wavelengths. The associated lineic attenuation coefficient is $\alpha_R = A.\lambda^{-4}$ with $A \sim 0.7\text{-}0.9 \text{ dB.km}^{-1}.\mu\text{m}^{-4}$. Rayleigh scattering is a stable linear elastic process, generated by material particles or defects of size much smaller (order of nanometer) than the propagating wavelength, that randomly re-emits photons in all directions and with conserved energy as illustrated in Figure 3. This diffusive process, applied to sunlight in the Earth atmosphere, is the reason for the blue color sky as well as the yellowish to reddish hue of the low sun. In silica glass, Rayleigh scattering is due to intrinsic local heterogeneities/impurities in the disordered material after fusion and manufacturing, with microscopic, random, and frozen variations of density and refractive index.

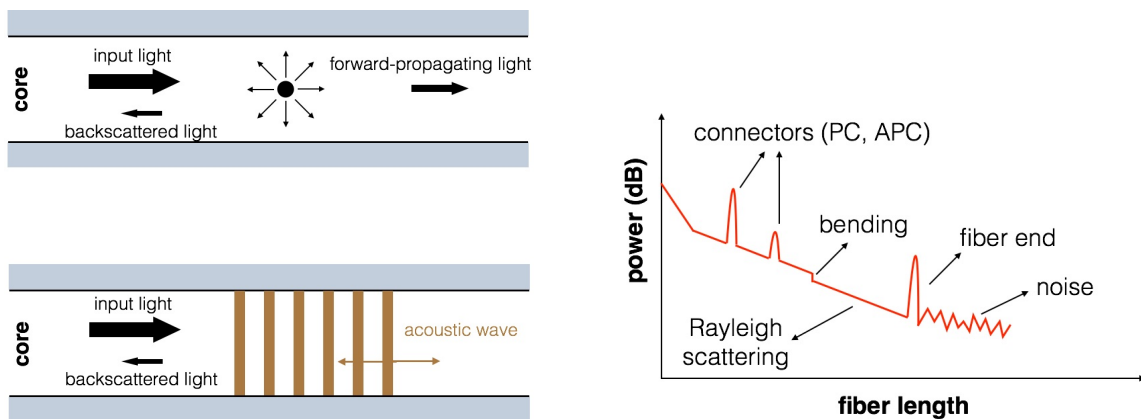


Figure 3. Schematic of Rayleigh (top left) and Brillouin (bottom left) scatterings, and typical curve of back-detected power as a function of time/distance (right, from [20]).

Additional intrinsic attenuation sources in silica fibers include Brillouin and Raman scatterings, with much lower effects than Rayleigh scattering (up to 20 dB and 30 dB weaker, respectively). They are very similar nonlinear scattering processes, corresponding to interactions between the incident light and vibrating silica molecules, that produce photons with frequency/energy shifts between incident and scattered waves. However, the shifts are much smaller in the Brillouin case (some GHz) than in the Raman case (some THz). Both refer to Stokes (resp. anti-Stokes) scattering when photons are emitted with lower (resp. higher) energy than the incident photon, with associated down-shifted (resp. up-shifted) frequency. On the one hand, the Raman scattering is due to thermal agitation (optical phonons) in Raman-active silica glass [190]. On the other hand, the Brillouin scattering is due to very small pressure waves i.e. acoustic phonons generated in the fiber core when the light intensity reaches a sufficient level [211]; these produce new down-shifted or up-shifted components depending on their direction of propagation (Doppler shift [104, 209, 172]), as illustrated in Figure 3. The latter scattering can occur in a spontaneous or stimulated manner: as long as the input light is scattered without strongly altering the properties of the medium, the Brillouin scattering is considered spontaneous, with acoustic waves generated by thermal noise; however, when the light intensity increases to a level such that the optical properties of the medium are modified with density change due to electrostriction, this scattering becomes stimulated by generated vibration waves [44, 52].

Rayleigh, Brillouin and Raman scatterings can be understood in terms of energy transfers between photons and material molecules (Figure 4). When absorbing an incident photon of frequency ν_0 (energy $h\nu_0$ with h the Planck constant), a molecule reaches a higher energy level with excited electron. This is a virtual unstable level, so that it can not stay for long on this level and makes almost immediately a transition toward a lower allowed energy level by emitting a new photon. The following cases can be exhibited depending on the scattering mechanism:

- from the ground state E_g , if the molecule energy performs the transition $E_g \rightarrow E_g + h\nu_0 \rightarrow E > E_g$ to an excited state, a photon of frequency ν_0 is absorbed and a lower-energy scattered photon of frequency $\nu_S < \nu_0$ is released; this corresponds to Raman-Stokes scattering ($\nu_S = \nu_0 - \nu_{opt}$) or Brillouin-Stokes scattering ($\nu_S = \nu_0 - \nu_a$), with additional creation of an optical (resp. acoustic) phonon with frequency ν_{opt} (resp. ν_a);
- from an excited state E , if the molecule energy performs the transition $E \rightarrow E + h\nu_0 \rightarrow E_g < E$ to the ground state, a photon of frequency ν_0 is absorbed and a higher-energy scattered photon of frequency $\nu_{AS} > \nu_0$ is released; this corresponds to Raman-anti-Stokes scattering ($\nu_{AS} = \nu_0 + \nu_{opt}$) or Brillouin-anti-Stokes scattering ($\nu_{AS} = \nu_0 + \nu_a$), with additional annihilation of a pre-existing optical (resp. acoustic) phonon with frequency ν_{opt} (resp. ν_a);
- from the ground state E_g , if the molecule energy performs the transition $E_g \rightarrow$

$E_g + h\nu_0 \rightarrow E_g$, a photon of frequency ν_0 is annihilated and a scattered photon of same frequency ν_0 (no shift) is created. This is elastic Rayleigh scattering.

Let us note that the frequency shift due to Brillouin scattering, associated with the energy of the absorbed or emitted acoustic phonon, reads $\nu_a = 2n_{eff}v_a/\lambda_0$, with n_{eff} the effective refractive index and v_a the acoustic velocity (speed of sound $\sqrt{E/\rho}$ function of Young modulus E and density ρ) in the fiber [171, 131]; for typical SMF fibers, with $v_a = 5,960$ m/s, $n_{eff} = 1.5$ and $\lambda_0 = 1,550$ nm, it yields a 11 GHz shift. As regards Raman scattering, the frequency shift is $\nu_{opt} \sim 13$ THz (about 100 nm wavelength shift) for a similar input wavelength.

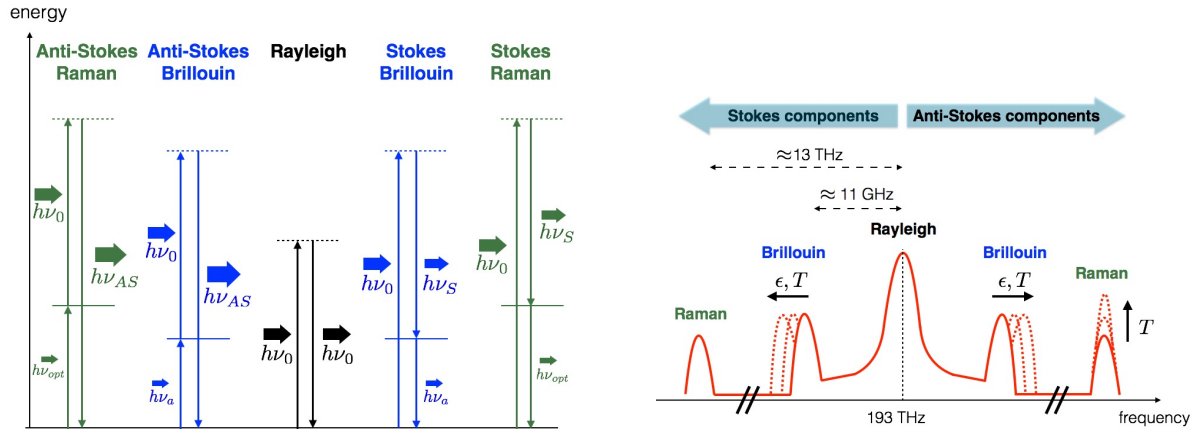


Figure 4. Schematic representation of energy exchanges for Rayleigh, Raman and Brillouin scatterings (left), and of the associated spectral components (right).

The resulting schematic representation of frequency spectra associated with Rayleigh, Raman and Brillouin scatterings is given in Figure 4, in an intensity vs. frequency diagram. It exhibits a central peak at the incident light frequency due to Rayleigh scattering, as well as down-shifted and up-shifted frequency peaks due to Raman and Brillouin scatterings.

2.3. Optical fibers as sensing elements

The previously described optical losses resulting from intrinsic scattering phenomena represent a drawback for transmission and communication, but are a major asset and are exploited for sensing with optic fibers. As a matter of fact, the scattered light that radiates in all directions is partially captured by the guiding structure of the fiber and back propagates to the fiber input; the fraction of captured optical power reads $\theta_0^2/4n_{core}^2$. This backscattered signal, rather weak in intensity (several tens of dB less than the incident signal) and generated by scatterings along the entire fiber length, presents a high repeatability and has a pattern that constitutes a unique fingerprint of the fiber for a given reference configuration and over a frequency range, as shown in Figure 3. It can be beneficially used for sensing when the fiber configuration changes, as features of

the backscattering signal are affected by local state variations. It can then be analyzed and compared, in the time or frequency domain, to the unperturbed configuration in order to obtain physical information e.g. on strain or temperature evolutions along the fiber. Some main aspects of the topic are described in the remainder of this section, with various sensing principles and techniques depending on the application.

2.3.1. Fiber Bragg gratings Apart from optic fiber sensing based on Rayleigh, Raman, or Brillouin scatterings which will be discussed later, we first briefly present the Fiber Bragg Grating (FBG) technology which is one of the most mature and commercially employed in optic fiber-based SHM. Producing multi-point though not distributed sensing, its principle leans on alterations of the fiber core in terms of a grating inscribed in a short segment of the fiber by means of an intense UV source. The grating pattern, usually periodic, results in a modulation in the core refractive index and generates a wavelength-specific dielectric mirror as dictated by Bragg's diffraction [118, 175, 231]. Therefore, it acts as a bandpass wavelength filter by reflecting a selected wavelength λ_{BG} of the injected broadband light signal while transmitting all others (Figure 5). This particular wavelength satisfies the following Bragg condition:

$$\lambda_{BG} = 2n_{eff}\Lambda_{BG} \quad (2.4)$$

with Λ_{BG} the grating period which is in the order of micrometer. In practice, the reflected spectrum is a narrow band centered at the wavelength λ_{BG} .

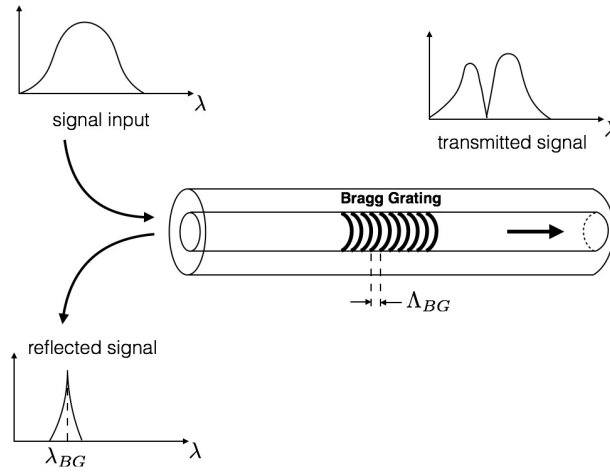


Figure 5. Illustration of the FBG principle.

When the fiber is affected by a change in longitudinal strain or temperature, parameters n_{eff} and Λ_{BG} change accordingly, which results in a shift in the reflected central wavelength as:

$$\frac{\Delta\lambda_{BG}}{\lambda_{BG}} = C_{\epsilon}^{BG} \Delta\epsilon + C_T^{BG} \Delta T \quad (2.5)$$

The strain coefficient

$$C_\epsilon^{BG} = \frac{1}{n_{eff}} \frac{\partial n_{eff}}{\partial \epsilon} + \frac{1}{\Lambda_{BG}} \frac{\partial \Lambda_{BG}}{\partial \epsilon} = 1 - p_e \quad (2.6)$$

depends on the photo-elastic coefficient p_e (~ 0.22 for silica), while the temperature coefficient

$$C_T^{BG} = \frac{1}{n_{eff}} \frac{\partial n_{eff}}{\partial T} + \frac{1}{\Lambda_{BG}} \frac{\partial \Lambda_{BG}}{\partial T} = \alpha_{n_{eff}} + \alpha_{\Lambda_{BG}} \quad (2.7)$$

depends on the thermo-optic coefficient $\alpha_{n_{eff}}$ ($\sim 6 \pm 3 \times 10^{-6} \text{ K}^{-1}$ for a germanium-doped silica core) and the fiber thermal expansion coefficient $\alpha_{\Lambda_{BG}}$ ($\sim 0.55 \times 10^{-6} \text{ K}^{-1}$ for silica). For a grating with a central wavelength at 1,550 nm, the typical temperature and strain sensitivities are then approximately 10 pm/°C and 1.2 pm/ $\mu\epsilon$. Consequently, interrogating a FBG with a wide spectrum light and retrieving the reflected spectrum enables to get information on the fiber mechanical and thermal state at the grating location. Moreover, several grating networks with their own features (length, refractive index distribution) may be inscribed in the same fiber to tend to quasi-distributed sensing, with a few mm resolution, using wavelength division multiplexing (WDM) techniques [155, 74, 241]; the process is however limited by the number of gratings that can be multiplexed in practice. A main drawback of FBS sensing is that it requires the *a priori* knowledge on critical locations to be able to position the gratings on the fiber. Over recent years, hybrid methods based on the simultaneous use of FBG sensors and piezoelectric actuators with propagation of elastic waves have also been investigated [21].

2.3.2. Raman-based DOFS Raman backscattering in optic fibers can be used for distributed temperature sensing (Raman Distributed Temperature Sensor, RDTS) as it is sensitive to temperature variations. Indeed, the associated amplitudes of Stokes/anti-Stokes components differently evolve with temperature; more anti-Stokes photons are produced when temperature increases [96], as the anti-Stokes process requires a pre-existing optical phonon generating a molecule with higher vibrational energy level before scattering, which is more likely to occur at higher temperature as described by Boltzman's distribution. On the other hand, the Raman-Stokes signal is weakly temperature-dependent. After sending a pulse from a pump laser source, the measurement at the input fiber end of the ratio of intensities between anti-Stokes (I_{AS}) and Stokes (I_S) backscattered components thus enables to deduce the temperature along the fiber. This ratio reads:

$$R(z, T) = \frac{I_{AS}(z, T)}{I_S(z, T)} = \left(\frac{\nu_{AS}}{\nu_S} \right)^4 e^{-\frac{h\nu_{opt}}{kT} - \int_0^z (\alpha_{AS}(u) - \alpha_S(u)) du} \quad (2.8)$$

with α_{AS} (resp. α_S) the attenuation coefficient associated with the up-shifted anti-Stokes (resp. down-shifted Stokes) backscattered component, k the Boltzmann constant, ν_{opt} the frequency of the annihilated or created optical phonon, z the position in the fiber,

and T the temperature at position z (in K). Comparing with ratios $R(z, T_0)$ at a reference temperature T_0 , this yields:

$$T(z) = \left[\frac{1}{T_0} - \frac{k}{h\nu_{opt}} \ln \left(\frac{R(z, T)}{R(z, T_0)} \right) \right]^{-1} \quad (2.9)$$

RDTs thus convert scattered light intensity variations into temperature variations. From reflectometry principles [95] with the link $2z = v\Delta t$ between position z in the fiber, propagation speed $v = c_0/n_{eff}$, and time delay Δt between emission and reception of laser pulses with roundtrip path (so-called time of flight), recording the ratio R as a function of time permits to deduce the features of Raman scattering along the fiber, and to construct a map of the temperature field. The typical temperature resolution is 0.01 °C, to be compared with typical resolution of frequently used thermocouple type K probes (~ 0.1 °C) or common medium wave infrared cameras in adequate condition of use (~ 0.02 °C).

Backscattered Stokes and anti-Stokes signals are in practice split by optic filters (selecting the wavelength) then sent to two detectors. Also, due to low efficiency of the mechanism as the light that is backscattered is scarce, a Raman interrogator generally uses multimode (MMF) fibers with higher power to maximize the amount of return light and simplify the measure. Moreover, it is usually necessary to perform averages in time, so that Raman-based systems are more suited for measuring slowly varying temperatures. First RDTs systems were proposed in [73, 51], and some reviews can be found in [34, 183, 189].

2.3.3. Brillouin-based DOFS Contrary to the previous intensity-based RTDS, optic fiber sensing from Brillouin backscattering relies on the analysis of the reflected frequency spectrum, and yields information on both strain and temperature quantities. As stated above, the intensity of Brillouin backscattering is maximal when the frequency shift with respect to the incident signal frequency corresponds to the value (so-called Brillouin central frequency):

$$\nu_B = \frac{2n_{eff}v_a}{\lambda_0} \quad (2.10)$$

Brillouin backscattering, caused by the propagation of density fluctuations of the medium with periodic change of the refractive index, can actually be seen as a moving Bragg grating. The central frequency ν_B , through silica glass properties (refractive index, density), is thus sensitive to strain and temperature variations occurring in the fiber. It linearly changes as [110]:

$$\Delta\nu_B = C_\epsilon^B \Delta\epsilon + C_T^B \Delta T \quad (2.11)$$

with standard sensitivity coefficients for SMF in the order of $C_\epsilon^B = -0.05$ MHz/ $\mu\epsilon$ and $C_T^B = -1$ MHz/°C for incident wavelength $\lambda_0 = 1,550$ nm and with classical properties of silica glass. Consequently, by measuring the distributed Brillouin frequency shift along the fiber, it is possible to estimate the optical fiber temperature and deformation conditions precisely. This may be performed in a spontaneous or stimulated manner,

corresponding to a natural or forced propagation of the acoustic wave respectively. In addition, it may be performed in the time domain by sending optical pulses, or the frequency domain to localize variations of strain or temperature along the fiber. In the former case, as Brillouin scattering is weak compared to Rayleigh scattering, reflexions from a number of pulses must be summed together to perform the measurement, so that the maximum frequency range for measurement is typically a few tens of Hz. Also, in direct detection and due to a quite small frequency shift, the Brillouin signal must be optically separated from the Rayleigh signal using an interferometer or a narrow bandwidth FBG filter. An alternative is to use heterodyne detection with a higher sensing range and better performance [213, 119].

Various Brillouin-based DOFS configurations have been implemented over the years. Using measurements in the time domain, we may list Brillouin Optical Time Domain Reflectometry (BOTDR) using spontaneous Brillouin scattering of a single laser pulse with amplification from a second continuous laser source [134, 110, 178], and Brillouin Optical Time Domain Analysis (BOTDA) using stronger stimulated Brillouin scattering with counter-propagating pulsed and continuous frequency-varying waves [109, 133, 110]. Both have limited spatial resolution (typically ≈ 1 m in classical systems) due to acoustic phonons lifetime [205] and extremely low intensity of the backscattered light, which require a minimal pulse width. Using measurements in the frequency domain, we refer to Brillouin Optical Correlation Domain Analysis (BOCDA) with correlation control between two frequency-modulated and counter-propagating optical waves [97, 111, 222], to Brillouin Optical Frequency Domain Reflectometry (BOFDR) [164], or to Brillouin Optical Frequency Domain Analysis (BOFDA) with sinusoidally-modulated input signal [80, 30, 31]. These latter improve the signal-to-noise ratio (SNR) and have increased spatial resolution at cm level. Advanced complex schemes and algorithms, such as PPP-BOTDA (Pulse-Pre Pump version with pre-impulsion of lower intensity) [135] or DP-BOTDA (Differential pulse version) [140], have more recently been implemented to always improve SNR and resolution [137, 192, 144, 210, 253, 168, 19, 248, 113]. Some reviews on Brillouin-based DOFS can be found in [17, 79, 167].

2.3.4. Rayleigh-based DOFS Randomly spread fluctuations of the refractive index in the core, that generate Rayleigh scattering, can be seen as a long weak Bragg grating with a random variation of amplitude and phase (i.e. random path along the fiber) [77]. This random Bragg grating model is valid as only the reflection components in the exciting wavelength range are detected. Referring to the Bragg condition, any change in the local optical path i.e. in the relative physical positions of the scattering centers modifies the locally reflected spectrum, with spectral shift in the backscattered pattern and consequently stretch in the overall reference fingerprint. Therefore, Rayleigh backscattering is also sensitive to both strain and temperature variations, and measuring the associated spectral shifts from the stored reference optic fiber signature (sensing baseline) provides distributed temperature or strain information. In the perturbed state,

correlating the signature indicates a spectral shift given by:

$$\Delta\nu_R = C_\epsilon^R \Delta\epsilon + C_T^R \Delta T \quad (2.12)$$

where standard sensitivity coefficients for Ge-doped SMF ($\nu_R \approx 193$ THz) are in the order of $C_\epsilon^R = -0.15$ GHz/ $\mu\epsilon$ and $C_T^R = -1.5$ GHz/ $^\circ\text{C}$.

In practice, techniques working in the time domain (Optical Time Domain Reflectometry – OTDR) or in the frequency domain (Optical Frequency Domain Reflectometry – OFDR) can be used to analyze the spectral shift; they are presented in further details in the next section. Compared to Brillouin-based DOFS, Rayleigh-based DOFS offers a shorter measurement range potential limited to few hundreds of meters, but it provides measurements with a much higher spatial resolution that permits the detection of damage or cracks. Also, Rayleigh backscattering permits the measurement of static and dynamic strains with short acquisition time, contrary to FBG or Brillouin backscattering which are limited to 1Hz sensing frequency or less.

As a remark, we mention that variations of light polarization and phase may also be exploited in Rayleigh-based sensing. The former is mainly used to measure the magnetic field or pressure through cross-section deformation (P-OTDR [197, 123], P-OFDR [176]). The latter, when involving a light signal with narrow bandwidth and stable frequency (with coherence length much longer than the fiber length), is usually employed to measure vibrations or acoustic waves from interference phenomena (Φ -OTDR [116, 246, 191, 151, 20]). The associated technologies, out of the scope of the SHM applications targeted here, will not be much addressed in the remainder.

To conclude this section, and out of compensation with additional strain-free fiber sensor [227] or mix of fibers with various properties [58], we mention that hybrid sensing schemes such as Raman-Brillouin or Brillouin-Rayleigh configurations can be used to address cross-sensitivity and discriminate between strain and temperature measurements [3, 61, 259, 128, 226]. For instance, a spatial resolution of both spontaneous Raman and Brillouin backscattered anti-Stokes signals is performed in [3]; once the temperature has been determined from the Raman signal, the strain can then be computed from the frequency measurement of the Brillouin signal. In [259], the Brillouin frequency shift (measured with BOTDA) and Rayleigh backscattering spectrum shift (measured with OFDR), both functions of temperature and strain, are used as independent information to discriminate between the two physical quantities; accuracies of $\pm 1.2^\circ\text{C}$ in temperature and $\pm 15\mu\epsilon$ in strain are reported with a measurement range of 92 m and a spatial resolution of 50 cm.

Also, strain and temperature discrimination methods by cross-correlation of Rayleigh backscattering spectrum shifts [78] or polarization sensitive OFDR [142] were investigated. In the latter case, a high accuracy simultaneous measurement of temperature and strain within 0.8°C and $7\mu\epsilon$ errors was achieved with spatial resolution of 6.5 mm over a 170 m fiber. More recently, a discrimination method combining conventional Φ -OTDR and Φ -OTDR-based birefringence measurements was proposed

in [152], with measurement uncertainties of 0.04°C and $0.5\mu\epsilon$. Nevertheless, the discrimination of strain and temperature measurements with DOFS remains a technical problem, which requires the development of additional techniques before being fully solved.

3. Working principles and technologies in Rayleigh backscattering-based sensing

In this section, we analyze DOFS solutions using the Rayleigh backscattering which are increasingly employed for SHM. We focus on the employed sensing processes, and associated technologies, all based on the comparison with an initially measured and stored Rayleigh scattering pattern (fiber signature) stemming from a reference state. We compare performance of various solutions in terms of measurement range, spatial resolution, and sensitivity (related to SNR) which are main features of DOFS sensors. We describe up-to-date Rayleigh-based sensing systems, even though new technologies using Rayleigh backscattering are continuously developed for sensing solutions with always improved performance.

The maximal measurement range of the sensing system occurs when the amplitude or content of the backscattered signal becomes so weak that it is impossible to obtain relevant information from them. Regarding the spatial resolution (or gage pitch/gauge length), it represents the spatial accuracy with which the measured physical field can be mapped. As a sharper spatial resolution deteriorates the measurement range, a compromise should be searched and can be quantified by the ratio between measurement range and spatial resolution, which can be interpreted as the number of equivalent sensing points offered by the fiber; it may be as high as some thousands. Measurement noise, coming from a variety of sources (laser noise, electronic noise, detector noise, ...), is also an important factor. It impacts the dynamic range (difference between the reference backscattered energy level and the noise level) and sensitivity (in terms of SNR ratio). Eventually, let us note that sensing from Rayleigh backscattering requires a specific device (terminal) at the fiber end, in addition to connection to the interrogation unit; its purpose is to prevent strong signal back-reflections from the end of the fiber that would interfere with and pollute the Rayleigh signal.

3.1. OTDR technologies

Optical Time-Domain Reflectometry (OTDR) from Rayleigh backscattering was developed in the late 70s [23, 24, 9] for fault detection, in terms of magnitude and location, in fiber telecom applications; its first use for distributed sensing can be found in [93]. It is the most common and simple reflectometry technique. In traditional Rayleigh OTDR [224], a pulsed laser source sends successive pulses to probe the sensing fiber, scattering sites (heterogeneities) within the fiber cause it to act as a distributed weak reflector, and the backscattered light intensity is collected in time at the input end

of the fiber then analyzed. The experimental setup is described in Figure 6. Practically, a laser source is electro-optically modulated to generate short optical pulses. It is a broadband laser source (linewidth ≈ 0.1 nm), so that the coherence length is less than the pulse width, and the detected signal represents intensity addition instead of field addition (no interference). The pulses are sent into the fiber through a circulator, and the intensity of the backscattered light is measured by a photodetector as a function of time then analyzed with a data acquisition device. When a pulse has had time to travel the full length of the fiber and back, the next laser pulse can be sent, avoiding reflections from various pulses and fiber sections at the same time which would make the OTDR system not operate properly; the measurement frequency is thus naturally limited by the fiber length. Recorded changes in local Rayleigh patterns, in terms of frequency shift, between successive pulses and generated by a given region of fiber enable to recover local strain or temperature information. These correspond to changes in the optical path length between scattering centers of that section of fiber, and are linearly related to strain or temperature variations (see (2.12)). In practice, the reflected intensity is collected in the time domain before being converted in the frequency domain (using FFT) for frequency spectrum analysis. Then, cross-correlation with the reference fingerprint frequency spectrum is performed in order to retrieve measured quantities from (2.12).

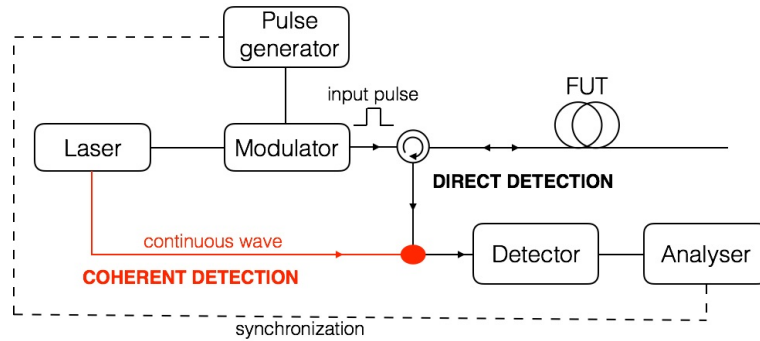


Figure 6. Experimental setup of typical OTDR (black) and COTDR (red) systems.

The spatial location z of backscattering events and changes along the fiber is again recovered from the relative time delay (time of flight) $\Delta t = 2z/v = 2n_{eff}z/c_0$ between the pulse launch and backscattered signal detection. It is obtained by means of a clock synchronization between the pulse generator and the data analyzer. A spatial trace of the backscattered signal can then be constructed and processed to extract information on the measured quantity.

As based on the time of flight, the spatial resolution of OTDR is determined by the duration τ_p of the transmitted optical pulse, as illustrated by the Minkowski diagram of Figure 7. Considering a rectangular pulse of width L_p in the fiber, occupying the space represented by the red segment at time $t = 0$, the detected signal at space-time point $(0, 2t_1)$ corresponds to the overlap of weak reflections from randomly spaced scattering

centers in the fiber portion between positions z_2 and z_1 (grey zone in Figure 7); signals can be summed coherently as the spacing between scattering centers is much smaller than the optical wavelength. The spatial resolution, corresponding to the smallest distance between two scattering centers that can be resolved, thus reads:

$$\Delta z_{min} = \frac{L_p}{2} = \frac{c_0 \tau_p}{2n_{eff}} \quad (3.1)$$

It can be improved by shortening the pulse width/duration, at the expense of (i) a broadened bandwidth of signal and photodetector (typically tens of GHz bandwidth for a millimeter-resolution) with increased dispersion and detection noise level, and (ii) a weakened pulse energy and consequently a lower backscattered signal. This procedure thus leads to a more difficult propagation and detection, and consequently to reduced measurement range and SNR (roughly proportional to the square of the spatial resolution) [99]. Reversely, enhancing the measurement range and SNR means increasing the backscattered energy and consequently the pulse width/duration as peak power is limited by undesirable distorting and even damaging nonlinear effects in the fiber, which decreases the spatial resolution. This trade-off between dynamic/measurement range and spatial resolution represents the fundamental limit of an OTDR system.

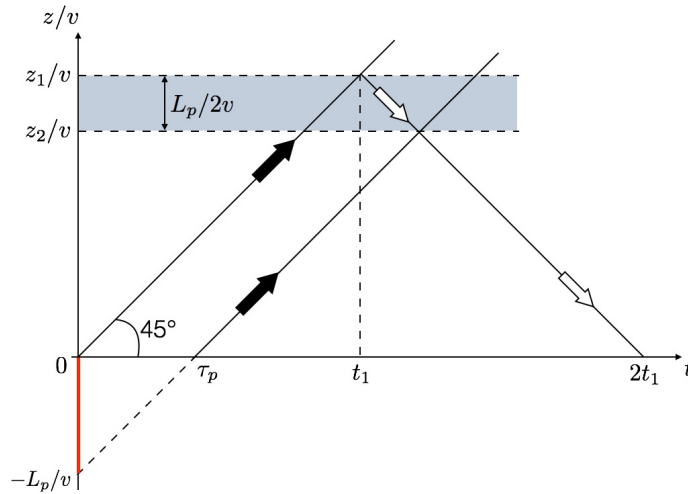


Figure 7. Minkowski diagram sketching the propagation of a probe pulse and of the corresponding Rayleigh backscattering.

A few techniques have been introduced to enhance the Rayleigh signal. We may mention coded-OTDR [115, 136] that uses several encoded pulses sent in the fiber at the same time, as well as technologies with photon-counting detectors that decrease noise and increase the OTDR dynamics [98, 158, 67]. Also, coherent detection (COTDR) rather than direct detection may be used to greatly increase the SNR and sensitivity of the naturally weak detected Rayleigh backscattering signal [262, 125, 182, 130, 159, 146]. The principle, similar to Φ -OTDR, consists of mixing the backscattered optical signal with part of the initial continuous laser source used as a local oscillator, before it reaches

the photodetector (see Figure 6). The detected signal thus becomes the interference between the local high-amplitude oscillator and the Rayleigh backscattered light, which is next demodulated. This technology requires a narrow linewidth (in the order of KHz) laser source for high coherence i.e. coherence length longer than the pulse length. One of its main drawbacks is its high sensitivity to phase noise as well as laser noise, as the laser frequency drift should be much smaller than the Rayleigh pattern change [212]. Alternatively, chirped pulses generated by tuning laser frequency can be used [180, 243] for scanned frequency OTDR trace; this refers to Tunable Wavelength Optical Time-Domain Reflectometry (TW-COTDR). By including multiple frequency components in a single pulse, local cross-correlation between trace segments (obtained from two consecutive measurements) is performed to recover frequency differences then sensing information.

In any case, OTDR techniques are limited in terms of spatial resolution for practical SHM applications. Indeed, they implement a pulse width at least of the order of $\tau_p \approx 10$ ns, which corresponds to a 1 m spatial resolution (with $c_0 = 3 \cdot 10^8$ m.s⁻¹ and $n_{eff}=1.5$). This well-known limitation may be reduced (few centimeters resolution) with specific recent techniques such as chaos-OTDR injecting light with random fluctuations in intensity [62]. It may be definitely overcome by alternative OFDR methods, presented in the next section, which enable to reach sub-millimeter spatial resolution, with extremely high dynamic range, sensitivity, and scan rate (hundreds of Hz [260, 256]) capabilities. For this reason, they have received much attention these last years in both research studies and engineering activities, and we make a specific focus on them in the remainder of the paper.

3.2. OFDR technologies

Alternative Rayleigh-based sensing approaches are based on a frequency-domain analysis, which actually represents the dual way of time-domain analysis. This refers to Optical Frequency-Domain Reflectometry (OFDR) in which the probe signal is a continuous frequency-scanned (chirp) optical wave instead of a pulsed signal [66, 127, 235]. Therefore, contrary to OTDR which measures the impulse response of the fiber by reading the intensity of the Rayleigh backscattered signal, OFDR consists in measuring its frequency response by analyzing interference fringes. A DOFS with high spatial resolution, using Rayleigh-based OFDR and so-called Optical Backscattered Reflectometer (OBR), was first developed in [77]. Also, a recent review on Rayleigh-based OFDR can be found in [59].

The basic experimental setup of conventional OFDR with coherent detection (C-OFDR) is shown in Figure 8. The light source is a continuous wave whose frequency is linearly swept with respect to time, in a bandwidth that extends to several tens of nanometers, e.g. in the band 1,535 nm-1,565 nm. It is generated by a tunable laser source (TLS). This input signal is split by a 90-10 coupler into probe and reference paths, then the

signal backscattered in the optic fiber sensor is coherently recombined in an output 50-50 coupler with the reference signal used as a local oscillator. The superposition of the reference frequency-modulated laser signal and time-delayed versions of it leads to interference at the coupler and results in a beating signal, with beats in the low-frequency range, which is further collected and analyzed after acquiring the amplitude and phase of the Rayleigh backscattering signature as a function of position in the fiber.

Using a linear optical frequency sweep around the laser central frequency, the measured beat frequencies (selected with bandpass filtering) can be easily mapped to the spatial domain, i.e. to the distance at which the backscattered signal occurred, as illustrated in Figure 8. Indeed, the proportionality factor between a beat frequency f_b and the corresponding time of flight Δt_z related to the backscattering position z (i.e. time delay between the backscattered light from the FUT and the reference light) corresponds to the frequency tuning rate. This rate is defined as $\gamma = \Delta f / T_s$, with T_s (resp. Δf) the frequency sweep time (resp. span). It consequently yields:

$$f_b = \gamma \Delta t_z = 2\gamma z \frac{n_{eff}}{c_0} \quad (3.2)$$

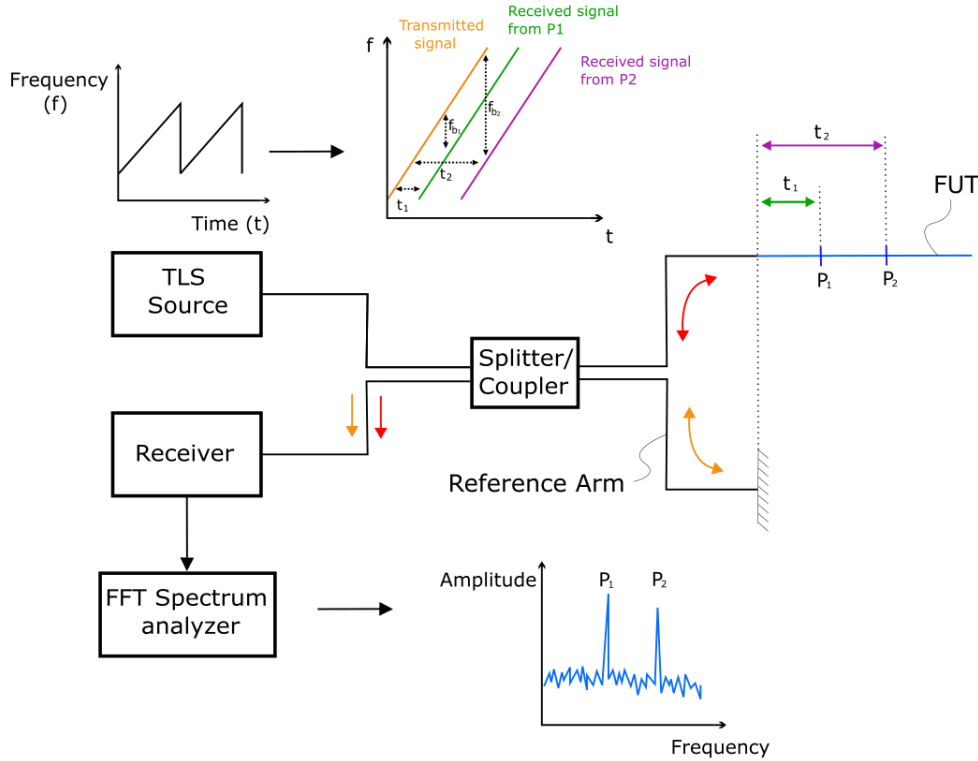


Figure 8. Operation principle of C-OFDR using interferometry.

In practice, the signal processing is as follows (see Figures 8 and 9):

1. the beat measurement signal, with simultaneous reception of signals backscattered along the fiber (parallel interrogation), is acquired in the optical frequency domain

after applying FFT. We notice again that performing this procedure on the fiber in its reference state provides a unique fingerprint (Rayleigh backscattering signature (RBS)), and that this fingerprint is shifted when the fiber is altered by temperature or strain, as predicted by (2.12);

2. the frequency signal is transformed to the spatial domain by performing another FFT (wavenumber response) and is then divided into short segments, of the order of millimeters or centimeters, using a sliding analysis window of length Δx which indicates the spatial resolution of the method;
3. each windowed Rayleigh backscattering pattern, associated to a specific fiber segment, is transformed back (using inverse FFT) to the optical frequency domain as a backscattering spectrum with frequency peaks. This corresponds to splitting by bandpass windowing in the frequency domain;
4. cross-correlation between local measured spectra and fingerprint (reference in the baseline state) spectra is operated, optical frequency shifts being given by shifts of cross-correlation;
5. the spectral shift in each segment is linearly converted into temperature or strain changes using (2.12), and is associated with a specific measurement location, leading to distributed measurements along the fiber.

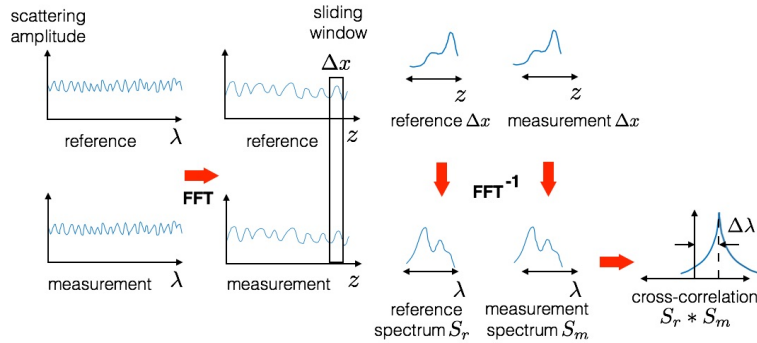


Figure 9. Dividing the signal into Δx windows, and cross-correlation (from [59]).

With this process, the minimal spatial resolution is determined by the frequency range of the laser; it reads from Fourier transform:

$$\Delta z_{min} = \frac{c_0}{2n_{eff}\Delta f} \quad (3.3)$$

It can be at the millimeter level when using a few tens of nanometer wavelength sweep range [221], even though it does not represent a physical boundary but a limitation in data processing devices. It of course decreases when the measurement rate is increased (as Δf is lower, for fixed tuning rate γ).

In practice, the sliding window may contain N data points, so that its size reads

$\Delta x = N\Delta z_{min}$ and corresponds to an effective sensing spatial resolution (gauge length). As regards the optical frequency resolution in the system, it is given by:

$$\delta\nu_{min} = \frac{\Delta f}{N} = \frac{c_0}{2n_{eff}\Delta x} \quad (3.4)$$

and is directly related to minimal measurable sensed quantity variation through sensitivity coefficients in (2.12). It shows that the minimal measurable sensing variation can be decreased by increasing Δx .

In addition, and in contrast to OTDR, an OFDR system has relatively higher power per frequency component, with lower receiver bandwidth which can be reduced down to the MHz level, so that an enhanced SNR is obtained. Also, let us notice that a high tuning rate is an important factor to achieve dynamic measurements.

Eventually, let us also mention some recent works e.g. [257] in which OFDR measurement is performed from phase analysis of the interference signal (Φ -OFDR), rather than intensity correlation. Considering again a TLS with linear optical frequency sweep at tuning rate γ , the optical signal $E_r(t)$ coming from the reference path and the signal $E_s(t)$ back-reflected at position z along the fiber are respectively written as:

$$E_r(t) = E_0 \cos\left(2\pi(\nu_0 t + \frac{1}{2}\gamma t^2)\right) \quad ; \quad E_s(t) = \sqrt{R_z} E_r(t - \Delta t_z) \quad (3.5)$$

with R_z the reflectivity at position z . The resulting interference signal magnitude then reads:

$$I_z(t) = 2E_0^2 \sqrt{R_z} \cos\left(2\pi(\nu_0 \Delta t_z + \gamma \Delta t_z t - \frac{1}{2}\gamma \Delta t_z^2 + \phi(t) - \phi(t - \Delta t_z))\right) \quad (3.6)$$

Introducing the initial phase $\phi_z = \nu_0 \Delta t_z - \frac{1}{2}\gamma \Delta t_z^2 + \phi(t) - \phi(t - \Delta t_z)$, it is shown in [257] that a change $\Delta\phi_z$ in this phase can be related to a local variation of the fiber length, so that strain can be recovered from the computation of $d\Delta\phi_z/dz$.

In any case, the maximal measurement range in C-OFDR is limited by the laser coherence length that should be comparable to the sensing fiber length, for sound interferometry. It should actually be at least four times longer, due to roundtrip propagation and Shannon's theorem (indicating that the sampling rate should be higher than twice the frequency range). Beyond the coherence length, laser phase noise induces random phase changes at scattering positions along the sensing length, and therefore measurement noise with low scattering signature repeatability and degraded SNR and spatial resolution. Consequently, the sensing length may reach a few tens of meters only, preventing measurements on large structures [179]. It can be increased to few hundreds of meters or some kilometers by using expensive and not commonly available laser sources with long coherence length, by introducing nonlinear phase noise compensation (by software processing) to perform measurement beyond the laser coherence length [68, 114, 57, 63, 223], or by using other advanced procedures [13, 174, 240].

In addition, linear sweep conservation should be carefully controlled for accurate measurement [166, 252]. However, the measurement accuracy is also largely limited by

several factors, including the cross-correlation accuracy in the spectral domain, ambient temperature fluctuations that generate nonlinearities in frequency sweep, and quality of the intensity detector (instrument accuracy). At short gauge length Δx (i.e. in the order of millimeters), cross-correlation uncertainty is dominating, while the other two noise components become major factors as the gauge length becomes larger.

As an alternative to coherent OFDR described before, based on interferometry and thus highly dependent on the laser coherence properties, incoherent OFDR (I-OFDR) techniques with intensity and frequency modulation of continuous waves and possibly specific hardware signal processing e.g. with Kerr phase-interrogator have been developed [169, 236, 145, 16]. They intrinsically enable a much longer sensing length (few tens of kilometers without any amplification), but with much less spatial resolution and sensitivity.

Nowadays, Rayleigh-based OFDR techniques are the most performing in commercially available systems. They enable to reach high spatial resolution and acquisition rate compared to alternative techniques. This is however compensated by a short measurement range; for long sensing distances, i.e. several tens of kilometers as in classical civil engineering applications, Brillouin-based techniques should be preferred at the expense of a broader spatial resolution.

Performance of a typical and up-to-date Rayleigh-based OFDR system is given in Table 1 below. This system corresponds to the ODiSI-6100 Series device (ODiSI refers to Optical Distributed Sensor Interrogator), commercialized by Luna Innovations [154] and shown in Figure 10. It is a multichannel (up to 8 channels) optic fiber interrogator, based on intensity cross-correlation in the frequency domain, with high spatial resolution (down to 0.65 mm) and acquisition frequency (up to 250 Hz, divided by the number of active channels). It uses optic fibers with length up to 10 m in its standard configuration, and up to 50 m in an extended configuration with signal amplification. The gage pitch (or gauge length) is software-configurable, while streaming data are displayed in real-time. Eventually, the system permits experimental configurations in which the measurement location is further remote from the monitoring unit.

We mention that measurement uncertainty given in Table 1 includes the effects of the instrument and sensor, and is equal to twice the standard deviation calculated from a set of 1,000 measurements. As regards system accuracy, it is here defined by comparison with extensometer measurements, based on average of 150 measurements at each of seven increments of strain (from 0 to maximum strain).

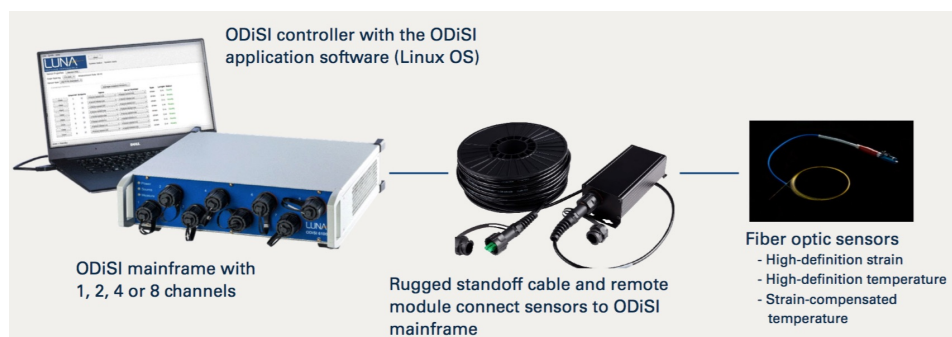


Figure 10. ODiSI-6100 Series device from LUNA Innovations [154].

Gage pitch		0.65 mm	1.3 mm	2.6 mm	5.2 mm
Gages per meter		1,538	768	384	192
Measurement rates	2.5 m mode	62.5 Hz	125 Hz	250 Hz	250 Hz
	5 m mode	40 Hz	80 Hz	160 Hz	160 Hz
	10 m mode	25 Hz	50 Hz	100 Hz	100 Hz
	20 m mode	12.5 Hz	25 Hz	50 Hz	50 Hz
	50 m mode	-	10 Hz	20 Hz	20 Hz
Strain measurement range		$\pm 15,000 \mu\epsilon$			
Resolution		$0.1 \mu\epsilon$			
Instrument accuracy		$\pm 1 \mu\epsilon$			
System (instrument & sensor) accuracy		$\pm 25 \mu\epsilon$	$\pm 30 \mu\epsilon$	$\pm 30 \mu\epsilon$	$\pm 30 \mu\epsilon$
Uncertainty at zero strain	Standard	$\pm 10 \mu\epsilon$	$\pm 6 \mu\epsilon$	$\pm 4 \mu\epsilon$	$\pm 4 \mu\epsilon$
	Extended range	$\pm 14 \mu\epsilon$	$\pm 7 \mu\epsilon$	$\pm 4 \mu\epsilon$	$\pm 4 \mu\epsilon$
Uncertainty across full strain range		$\pm 22 \mu\epsilon$	$\pm 16 \mu\epsilon$	$\pm 4 \mu\epsilon$	$\pm 4 \mu\epsilon$
Dynamic loading rate		1 Hz	2.5 Hz	5 Hz	5 Hz
Temperature measurement range		-40 to 200 °C			
Resolution		$0.1 \text{ } ^\circ\text{C}$			
Measurement uncertainty		$\pm 2.2 \text{ } ^\circ\text{C}$	$\pm 1.6 \text{ } ^\circ\text{C}$	$\pm 0.6 \text{ } ^\circ\text{C}$	$\pm 0.6 \text{ } ^\circ\text{C}$

Table 1. Performance of the ODiSI-6100 Series system.

As a comparison, a summary of typical performance currently offered by alternative distributed sensing techniques is reported in Table 2.

Sensing technology	Sensing range	Spatial resolution	Strain accuracy
Rayleigh OFDR	50-70 m	1 mm	$\pm 1\mu\epsilon$
Raman OTDR	1-40 km	1 cm-20 m	–
Brillouin BOTDR	20-50 km	0,1 m	$\pm 30\mu\epsilon$
Brillouin BOTDA	2-150 km	2 cm-2 m	$\pm 10\mu\epsilon$
Multiplexed FBG	≈ 100 channels	2 mm (Bragg length)	$\pm 1\mu\epsilon$

Table 2. Comparison of performance between several distributed sensing techniques.

4. Recent SHM applications and challenges with Rayleigh-based sensing

Despite its limited sensing range, Rayleigh-based OFDR provides a high spatial resolution which is ideal for structural strain mapping and localized damage detection and monitoring, provided a suitable network e.g. regular grid of fibers is used. Coming along with the availability of powerful commercial devices for implementation (data processing, laser, driver), it has become a mature technology and has given rise to many works describing applications in various fields, and in both research and industry. We detail some of them below, focusing on some representative SHM applications involving damage phenomena, but many others can be found in the literature, e.g. [42, 33, 161, 239, 105, 245, 203, 242], addressing the monitoring of various structural parameters. It is important to remind that Rayleigh-based OFDR is a rising but quite new technology for SHM systems, so that possibilities have just started to be grasped.

4.1. Some applications in civil engineering

A main application of Rayleigh-based OFDR sensing deals with the monitoring of concrete civil engineering structures, with several works reported in [81, 106, 237, 129, 195]. Some very recent applications can be found in [196] with the investigation of an experimental methodology to obtain the shear cracking pattern of reinforced concrete beams, in [27] where a OBR system technology is used on a real-world bridge structure, in [36] where the potential for monitoring a series of slender and deep reinforced concrete beams subjected to bending cyclic loading is addressed, in [117] where Rayleigh-based OFDR sensing is used in piles subjected to general subsidence, in [6] with several applications to textile-reinforced concrete materials, or in [32] for crack monitoring (crack location and width evolution over time) using thin polyamide-cladded fibers in reinforced concrete beams subjected to three-point bending tests. In several applications, the high spatial resolution resulted in a considerable number of spikes observed in a distributed strain profile, indicating the detection of cracking even at low load levels and when the cracking was still not visible (premature cracking).

As a typical illustration, we report here an application on reinforced concrete beams during a three-point load test given in [26]. Specimens had a 800 mm length, and 100 mm \times 180 mm cross-section, with only one reinforcing bar deployed at the center of the cross-section (Figure 11). The used fiber had a 5.2 m length and 155 μ m diameter, with single thin polyamide coating (no thick protection) to increase the reliability of the measurements. Part of the fiber was directly embedded in the rebar elements inside the concrete (segment FI), with bonding on the reinforcing bar using a cyanoacrylate or epoxy adhesive, while the remaining part of the fiber was glued to the surface after the concrete hardening (Figure 11). This configuration permitted a direct comparison between the developed strains on the concrete surface and the rebar from a single sensor. Also, it was also expected to detect and follow the evolution of cracking (with expected cracking around 10 kN) with the external segments. The fiber placement was such that it was possible to measure compression strains at the top lateral segment (FE-H1), about zero-value strains at the neutral axis in the middle lateral segment (FE-H2), and tension strains at the bottom lateral segment (FE-H3) and the two bottom exterior segments (BE-H1 and BE-H2). Three strain gauges were also installed in the rebar for comparison purposes.

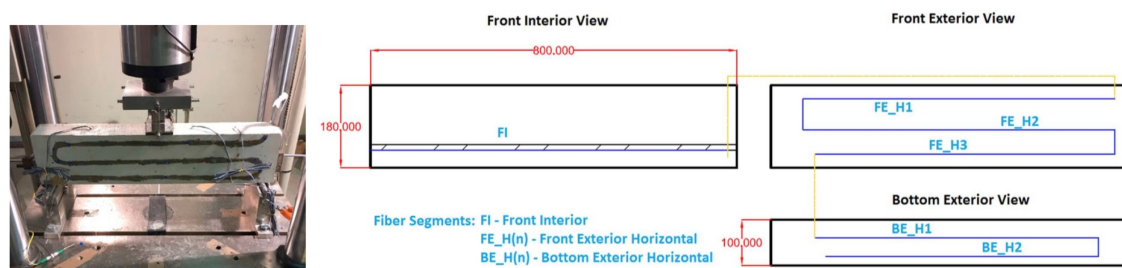


Figure 11. Beam specimen and DOFS deployment, from [26].

Measurements were conducted using a 1 cm spatial resolution, corresponding to more than 500 different measurement points along the fiber, with a 5 s interval between successive acquisitions. In addition, specimens were unloaded and reloaded again after cracking, in order to assess the capability of the fiber sensor when submitted to real risky loading scenarios that may damage it (roughness in the crack lips). Results for the first specimen (Beam 1) are shown in Figure 12. The expected concrete tensile strength capacity of 108 $\mu\epsilon$ was surpassed for a load of 7.5 kN, with crack detection and location on the beam surface from the DOFS even though it was not yet visually observable. Damage at the segment deployed in the rebar started being detected for a load of 10.81 kN. When analyzing each individual segment before the occurrence of cracking, it was possible to observe how the measurements smoothly followed the developed strains, with higher strains at mid-span as expected. From the segment (FI) adhered to the rebar, it was also possible to compare DOFS strains with the ones obtained by the strain gauges; a nice agreement between the two sets of sensors was achieved before the development of cracking, as shown in Figure 13.

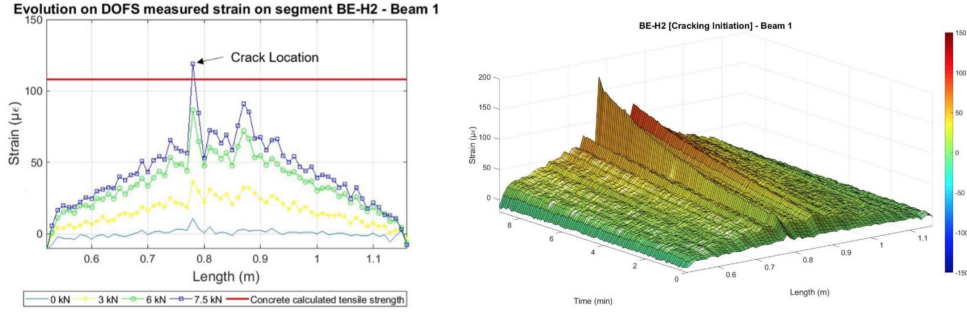


Figure 12. Detection of cracking at the surface of the concrete beam (left), and evolution of strains verified for segment BE-H2 (right), from [26].

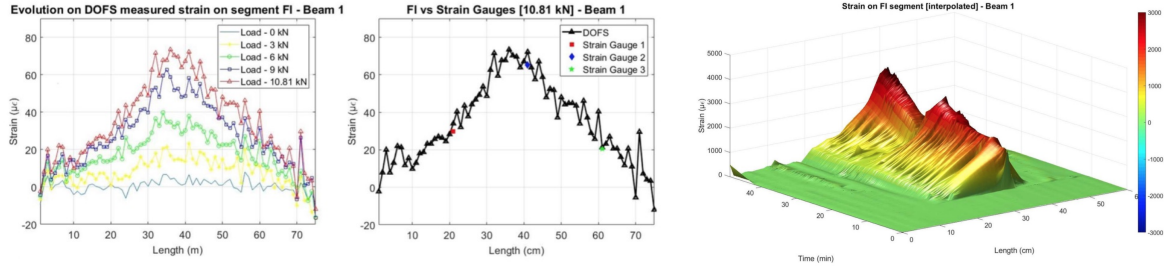


Figure 13. Strains measured by the DOFS on the embedded segment (left), and interpolated measured strain at the embedded segment (right), from [26].

Eventually, after cracking, a methodology was proposed to remove inaccurate measurements and interpolate based on the remaining accurate values. To select accurate values, the spectral shift quality (SSQ) of the measured data was analyzed. SSQ is a qualitative measure of the strength of the correlation between the conducted measurement (at any point and time) and the original baseline reflected spectra. It is defined as:

$$SSQ = \frac{\max_j [U_j(\nu) \otimes U_j(\nu - \Delta\nu_j)]}{\sum_i U_i(\nu) \otimes U_i(\nu)} \quad (4.1)$$

with $U_j(\nu)$ the baseline spectrum for a given segment j of data, $U_j(\nu - \Delta\nu_j)$ the shifted measurement spectrum due to strain or temperature change, and \otimes the cross-correlation operator. It should theoretically be between 0 (uncorrelated) and 1 (perfect correlation). In practice, any measurement with a SSQ below 0.2 was disregarded, as it is likely that the strain change has exceeded the measurable range when this threshold is reached. In addition, it was forecast that the further the damage would develop in the monitored structural element, the lower the SSQ values would be. The calculated values of SSQ for the beam measurements are shown in Figure 14. It was observed that the low SSQ values were close to the crack location in the segments adhered to the surface of the concrete and within a wider area in the rebar segment. This was explained as segments with large strain gradients increase the noise levels of the DOFS measurements. After

removing unreliable data points, it was then possible to interpolate the surface points of the embedded segment in order to better analyze the behavior of the structural element after cracking. Results in segment FI, shown in Figure 15, confirmed that after this post-processing the (interpolated) DOFS data mostly presented strain evolution which was compatible with the applied load, following the same cycle of loading, unloading and a new loading until the rupture of the fiber. Also, when comparing values after cracking with those measured by the strain gauges, a good agreement was observed as shown in Figure 15 for a load level of 15 kN. Furthermore, the crack visually observed on the beam specimen for this load level agreed with the data obtained by the sensors.

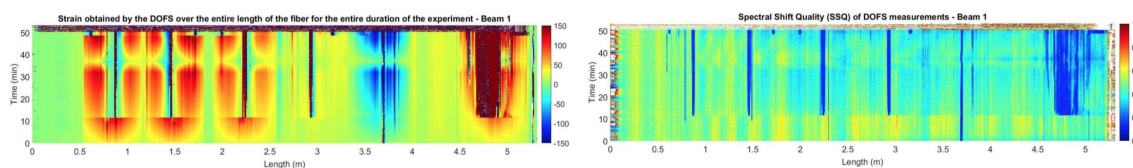


Figure 14. Strain and SSQ for the beam, from [26].

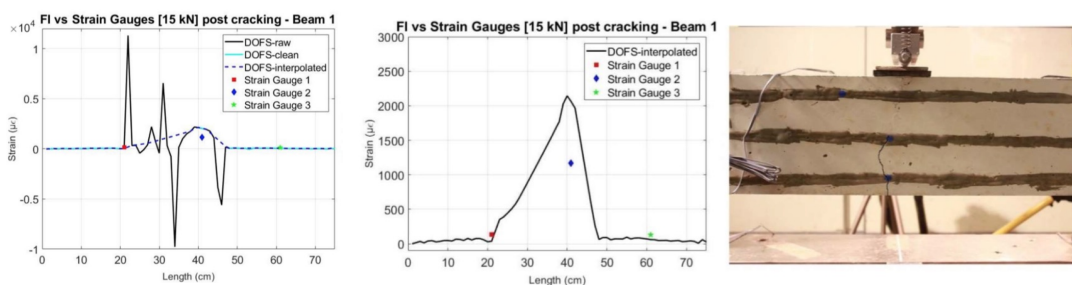


Figure 15. Comparison of the DOFS values (before and after interpolation) with strain gauges, and picture of the beam specimen with highlighted crack, from [26].

4.2. Some applications for composites in aeronautics

Another classical application of Rayleigh-based OFDR sensing deals with damage tracking and monitoring in high-tech composites structures used in aeronautics, with durability and safety issues. Composite materials indeed have a complex behavior, with damage initiation and propagation from various scenarios (delamination, transverse cracking, etc.) and in localized places (local impact, repair patches, lap joints). Due to their small size and flexibility, optical fibers can then be beneficially embedded in composites structures during the manufacturing layup process, for further strain mapping with spatial resolution down to a few millimeters, and thus effective local damage detection at large gradient locations. Several studies can be found in [206, 163, 186, 87, 85, 56, 217, 157, 216, 89].

A typical application was reported in [89], in which a cross-ply Carbon Fiber Reinforced

Plastic (CFRP) laminate was built from UD prepreg material, with an optical fiber embedded inside the laminate during layup (Figure 16). The laminate was then impacted by a drop weight test and a delamination was produced. The significant strains generated, with a peak of $300 \mu\epsilon$, and the delaminated length (25 mm) were perfectly depicted by an ultrasonic C-scan. The strain field map and the delaminated area were also obtained with relatively high accuracy by using DOFS and an optical fiber with crooked path placement, that is parallel segments every 5 mm.

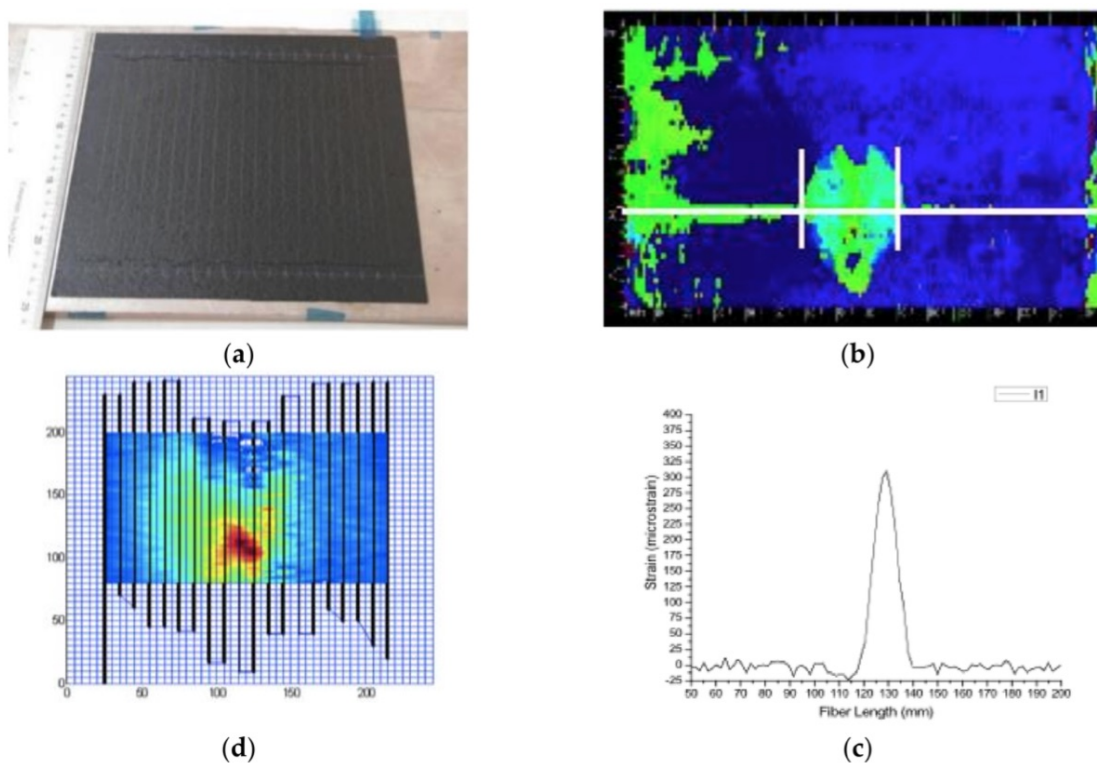


Figure 16. (a) Composite laminate with optical fiber following parallel paths; (b) Ultrasonic C-scan of the impacted laminate; (c) Strains measured by optical backscatter reflectometry along the white line (position of the optic fiber) of the upper figure; (d) Strain plotting at the delaminated area, obtained by parallel optical fibers, from [89].

4.3. Challenges

Rayleigh-based DOFS is becoming ubiquitous in SHM applications, and the market is expected to continue its growth with combination of academic research and industrial developments. Nevertheless, the technology is still recent and faces a number of issues and shortcomings which represent challenges to be addressed in the coming years, with additional tests (for a better understanding and analysis) and enhanced technical solutions. A major challenge is related to optic fiber integration in materials and structures. Despite being very small, a standard telecom fiber has a diameter which remains much larger than commonly used fibers (e.g. $5\text{-}10 \mu\text{m}$ for carbon fibers) in

composite materials with long-fiber reinforcement; it is rather of the order of a composite layer thickness. Even with reduced-diameter ($50\ \mu\text{m}$) fibers that have been developed for sensing purposes in aerospace structures [225], the difference is still of an order of magnitude. Consequently, it is likely that an embedded fiber affects the mechanical behavior, weakening material performance with additional interfaces [29], and acts as an unintended stress concentration and crack/delamination initiator due to the creation of resin pockets in the embedded fiber surrounding, as illustrated in Figure 17. The impact of a fiber on stiffness and strength properties may be evaluated by mathematical modeling and numerical methods, taking into account the layered structure, the types of layer stacking, the arrangement and respective orientations of layers and fibers. . . [65]. Nevertheless, several experimental observations indicated that optic fibers do not actually produce any significant modification of the mechanical properties in the host structure when suitably inserted. As long as the optic fiber is embedded between similar plies and the optical fiber is, predominantly, in the fiber direction of these plies, studies show that it has a minimally intrusive impact and the structure has little reduction in load capabilities [214]. In any case, the first track to guarantee the mechanical properties of composite materials used in smart structures passes through the closest possible encapsulation of the optical fiber between composite plies. Also, another difficulty may come from residual strains after manufacturing; the fiber is indeed subjected to the stress created at the boundary between the coating and the composite ply during the heating phase, which is only partially released during the cooling phase. Eventually, embedding fiber sensors in internal composite layers of a structure requires changing the existing mature manufacturing process and longer molding time, which will increase the manufacturing complexity and cost.

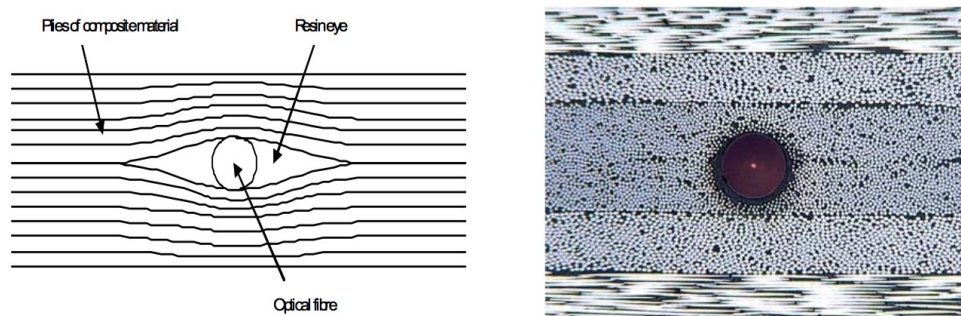


Figure 17. Sketch of the laminate cross section with resin eye (left), and optic fiber embedded parallel to reinforcement fibers in a tape laminate (right), from [88].

Another big challenge is sensing reliability and robustness, which may be affected by several factors:

- an optic fiber is relatively fragile (very poor shear resistance), in particular with thin coating. Among others, input and output points in the material are

critical locations due to severe bending experienced during manufacturing or under operating conditions, which may cause severe optical loss and fiber break [83]. Also, the installation phase is critical for the sensing fiber integrity. This aspect also refers to maintainability aspects, with the capability for replacement of damaged fiber sensors;

- in addition, when the fiber is glued on the structure surface, there may be issues with bonding adhesives for strain transfer (especially for thick coating), as reported in [28, 5, 14]. Therefore, a compromise actually needs to be found between measurement accuracy and protection and durability of the sensor when exposed to environmental conditions of real world applications;
- related to the previous points, some special packaging methods have been investigated in order to protect the fiber and increase its resistance in harsh environments. As recent advances, we may for instance cite [255] in which metallic-packaging FBG sensors have been developed, using an ultrasonic welding method, in order to bond polyamide-coated fibers to an aluminum alloy substrate. We may also cite [261] where a composite reinforcement in terms of carbon fiber reinforced polymer (CFRP) packaging is used with FPG sensors for strain monitoring of wind turbine blades, with sensing unit designed to maximize strain transfer.
- phase noise in OFDR should be conveniently managed, so that novel signal processing methods and algorithms, e.g. methods of nonlinear phase restoration, need to be explored to keep increasing sensing performance;

Alleviating these aspects appears mandatory to achieve the ultimate goal of establishing a standardisation framework for integration and certification of the technology in engineering structures, with a beneficial technological transfer to industry and fully mature readiness level.

Last but not least, some issues need to be addressed in order to enhance the practical relevance of DOFS sensing. One is the appropriate placement of fibers, to get the best coverage of the structure that has to be monitored and the best sensitivity to observed phenomena or identified parameters. Some preliminary studies in this direction can be found [141, 40, 7]. For instance, it was shown in [121] that sinusoidal positioning was a good option for various direction strain sensing. One could also imagine the deployment of a regular network of fibers when possible, in order to increase chances of detection in the close vicinity of a damage area. However, additional studies need to be conducted in order to define a consistent placement methodology.

Following the previous point, the association of DOFS with other advanced sensing techniques seems a relevant approach to optimize non-destructive sensing performance in real SHM applications. We may think of ultrasonic C-scan as reported in the application of Section 4.2; we may also think of DIC, whose integration inside a DOFS monitoring would permit complementary information without any interference, and with validation capabilities. Recent studies [160, 32] explicitly analyzed such a DOFS-DIC cooperation.

Another issue is in technical advancements, with the development of more powerful emission and reception devices (e.g. tunable laser sources with high tuning rate) so that dynamic measurements with high spatial resolution and measurement range can be performed. The current market requires acquisition rates in the range of up to 1 kHz. Also, the development of specific enhanced fibers to sense several quantities (not only physical, but also chemical or biological) with a single fiber is a current need.

Eventually, smart structures with damage detection and real-time monitoring capabilities not only need effective sensing technologies offered by DOFS (seen as a nervous subsystem), they also need to be effectively connected with powerful computing tools that would constitute the digital brain of the overall SHM system. These should permit robust data assimilation, explanation and processing, advanced simulation for diagnosis and prognosis, and reliable control as envisioned in the potentials of the DDDAS concept.

5. Conclusions

With this pedagogical review on DOFS systems for damage tracking and SHM, we covered main ideas on the involved physical backscattering principles, as well as practical implementation and instrumentation aspects that permit to recover the measured quantities of interest. We put a deeper focus on Rayleigh backscattering-based technologies which are nowadays the most attractive, due to their unique capabilities, for SHM applications of interest on medium-scale engineering structures. Nevertheless, as detailed in the last part of the work, major challenges remain to be addressed before this advanced technology becomes a standard in industrial activities.

Acknowledgments

This work has received funding from the European Research Council (ERC) under the European Union's Horizon 2020 research and innovation programme - ERC-2020-COG - ERC Consolidator Grant (grant agreement No. 101002857, DREAM-ON project).

Appendix A: Waveguide analysis

Appendix A.1. Case of a symmetric step-index planar waveguide

For the sake of understanding, we first consider a planar waveguide made of a guiding region of thickness d (of the order of the wavelength) in the direction x , and infinite in the other directions y and z (Figure A1). It is surrounded by a substrate and a superstrate (cladding) which are both semi-infinite along x . We assume linear, isotropic, charge-free, and current-free dielectric media. We also assume a step-index waveguide; although being invariant in y and z directions, the refractive index is n_1 within the guide ($-d/2 < x < d/2$) and n_2 outside the guide ($|x| > d/2$). The index variation along x is therefore described by a symmetric step function.

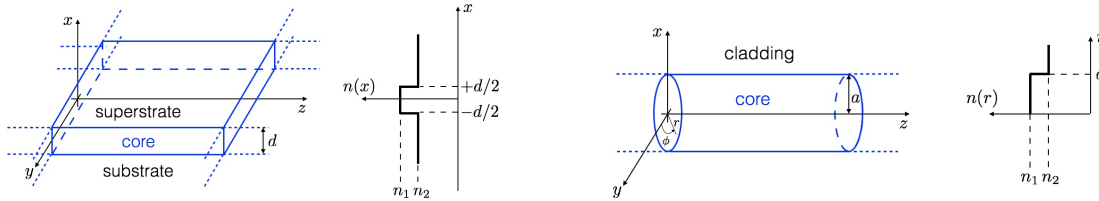


Figure A1. Scheme of the symmetric step-index planar waveguide with plot of its refractive index distribution $n(x)$ (left), and scheme of the step-index circular fiber waveguide with plot of its refractive index distribution $n(r)$ (right).

We choose z as the direction of propagation and look for guided modes, that are distributions of the electromagnetic field, of pulsation ω , that propagate along z without modification of their structure and vanish at $|x| \rightarrow \infty$. As a consequence of the invariance along y and z , electric and magnetic fields respectively read:

$$\mathbf{E}(x, y, z, t) = \text{Re}\{\mathbf{E}_0(x)e^{j(\omega t - \beta z)}\} \quad ; \quad \mathbf{H}(x, y, z, t) = \text{Re}\{\mathbf{H}_0(x)e^{j(\omega t - \beta z)}\}$$

where β is a propagation constant, related to the effective index n_{eff} as $\beta = n_{eff} \frac{\omega}{c_0} = n_{eff} k_0$ ($c_0 = 1/\sqrt{\epsilon_0 \mu_0}$). These fields should satisfy the following Maxwell equations:

$$\nabla \cdot \mathbf{D} = 0 \quad ; \quad \nabla \cdot \mathbf{B} = 0 \quad ; \quad \nabla \wedge \mathbf{E} = -\frac{\partial \mathbf{B}}{\partial t} \quad ; \quad \nabla \wedge \mathbf{H} = \frac{\partial \mathbf{D}}{\partial t} \quad (\text{A.1})$$

with $\mathbf{D} = \epsilon_0 n^2 \mathbf{E}$ and $\mathbf{B} = \mu_0 \mathbf{H}$ the electric displacement field and magnetic flux density, respectively. They yield 6 relations between fields components:

$$\begin{aligned} \beta E_{0y} &= -\omega \mu_0 H_{0x} \quad ; \quad \beta E_{0x} - j \frac{dE_{0z}}{dx} = \omega \mu_0 H_{0y} \quad ; \quad j \frac{dE_{0y}}{dx} = \omega \mu_0 H_{0z} \\ \beta H_{0y} &= \omega \epsilon_0 n^2 E_{0x} \quad ; \quad \beta H_{0x} - j \frac{dH_{0z}}{dx} = -\omega \epsilon_0 n^2 E_{0y} \quad ; \quad j \frac{dH_{0y}}{dx} = -\omega \epsilon_0 n^2 E_{0z} \end{aligned}$$

It is noticeable that these equations split into two independent sets of 3 equations, meaning that we shall have 2 families of guided modes. In the first set, the only non-zero field components are (E_{0y}, H_{0x}, H_{0z}) corresponding to transverse electric (TE) modes where the electric field \mathbf{E} has a single component along y while the magnetic field \mathbf{H} , orthogonal to \mathbf{E} , has longitudinal and transverse components (see Figure A2). Reversely,

the only non-zero field components in the second set are (H_{0y}, E_{0x}, E_{0z}) corresponding to transverse magnetic (TM) modes.

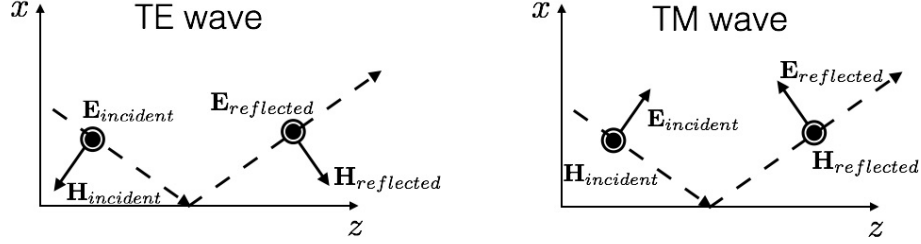


Figure A2. Respective positions of electric and magnetic fields for TE and TM waves.

Considering TE modes and combining equations, the propagation equation for the transverse electric field is found as:

$$\frac{d^2 E_{0y}}{dx^2} + [k_0^2 n^2 - \beta^2] E_{0y} = 0 \quad \text{with } k_0^2 = \epsilon_0 \mu_0 \omega^2 = \left(\frac{2\pi}{\lambda_0}\right)^2$$

Moreover, continuity equations $\mathbf{n}_{12} \wedge (\mathbf{E}_1 - \mathbf{E}_2) = \mathbf{0}$ and $\mathbf{n}_{12} \wedge (\mathbf{H}_1 - \mathbf{H}_2) = \mathbf{0}$ at the interface between domains 1 and 2 indicate that tangential components E_{0y} and H_{0z} (or dE_{0y}/dx) should be continuous at boundaries $x = \pm d/2$.

Electromagnetic waves may be guided, i.e. vanishing when $|x| \rightarrow \infty$, only when the longitudinal propagation constant β lies in the interval $k_0 n_2 < \beta < k_0 n_1$ (guidance condition), that is $n_{eff} \in]n_2, n_1[$. When this is fulfilled, the propagation equations can be rewritten as:

$$\begin{aligned} \frac{d^2 E_{0y}}{dx^2} + \alpha^2 E_{0y} &= 0 \quad \text{in the waveguide } (|x| < d/2) \\ \frac{d^2 E_{0y}}{dx^2} - \kappa^2 E_{0y} &= 0 \quad \text{outside the waveguide } (|x| > d/2) \end{aligned}$$

where we introduced the transverse propagation coefficient $\alpha^2 = k_0^2 n_1^2 - \beta^2 > 0$, and the extinction coefficient $\kappa^2 = \beta^2 - k_0^2 n_2^2 > 0$. Meaningful solutions, decaying at $x = \pm\infty$, then read:

$$\begin{aligned} E_{0y}(x) &= A \cos(\alpha x) + B \sin(\alpha x), \quad \text{for } |x| < d/2 \\ E_{0y}(x) &= C e^{\kappa x}, \quad \text{for } x < -d/2 \\ E_{0y}(x) &= D e^{-\kappa x}, \quad \text{for } x > d/2 \end{aligned}$$

On the one hand, symmetric TE guided modes correspond to:

$$E_{0y}(x) = A \cos(\alpha x) \quad \text{for } |x| < d/2 \quad ; \quad E_{0y}(x) = C e^{-\kappa|x|} \quad \text{for } |x| > d/2$$

and continuity conditions yield:

$$A \cos\left(\alpha \frac{d}{2}\right) = C e^{-\kappa \frac{d}{2}} \quad ; \quad \alpha A \sin\left(\alpha \frac{d}{2}\right) = \kappa C e^{-\kappa \frac{d}{2}}$$

A condition for this set of equations to provide a non-trivial solution is:

$$u \tan u = \sqrt{\left(\frac{V}{2}\right)^2 - u^2} \quad (\text{A.2})$$

where we introduced the dimensionless variables $u = \alpha d/2$ (reduced transverse propagation coefficient), $v = \kappa d/2$ (reduced extinction coefficient), and $V = k_0 d \sqrt{n_1^2 - n_2^2}$ (reduced frequency), with $u^2 + v^2 = \left(\frac{V}{2}\right)^2$.

On the other hand, antisymmetric TE guided modes correspond to:

$$E_{0y}(x) = B \sin(\alpha x) \quad \text{for } |x| < d/2 \quad ; \quad E_{0y}(x) = C \operatorname{sgn}(x) e^{-\kappa|x|} \quad \text{for } |x| > d/2$$

and continuity conditions yield:

$$B \sin\left(\alpha \frac{d}{2}\right) = C e^{-\kappa \frac{d}{2}} \quad ; \quad \alpha B \cos\left(\alpha \frac{d}{2}\right) = -\kappa C e^{-\kappa \frac{d}{2}}$$

A condition for this set of equations to provide a non-trivial solution is:

$$-u \cot u = \sqrt{\left(\frac{V}{2}\right)^2 - u^2} \quad (\text{A.3})$$

For each value of V , satisfying the dispersion relation (A.2) or (A.3) determines a discrete set of possible values for u and therefore for the propagation constant β , as shown in Figure A3. For any value of V , we observe that there is always at least one mode of the symmetric type with $0 \leq u \leq \pi/2$; it is called the fundamental mode, and corresponds to the smallest possible α i.e. minimal oscillation within the planar guide. It is the only mode allowed for small values of V . When V is further increased from zero, additional modes numbered by the integer m become allowed.

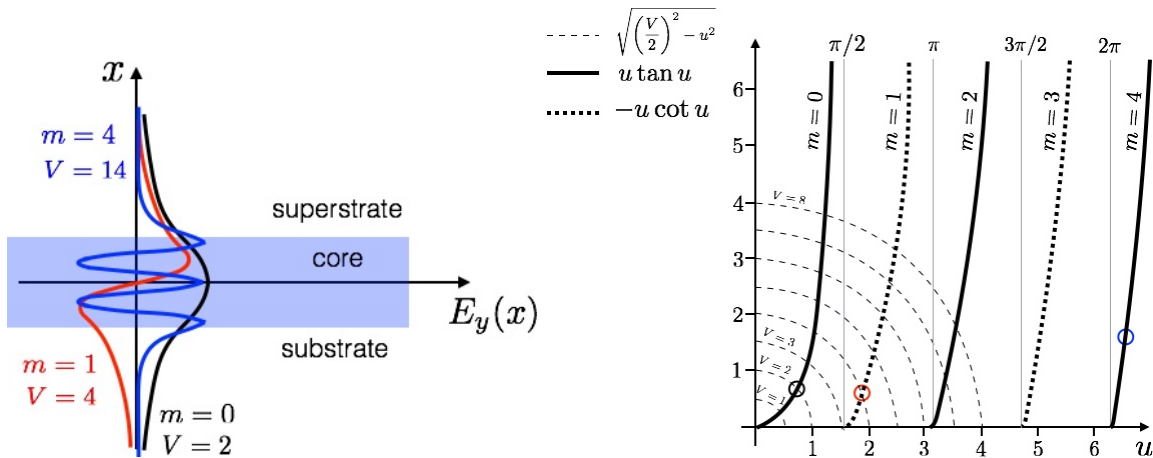


Figure A3. Illustration of modes for a symmetric step-index planar waveguide (left), and graphical determination of $u(V)$ (right).

For a given TE mode m , one may define a cut-off frequency $V_c^{(m)}$ such that the mode does not exist if $V < V_c^{(m)}$; it reads $V_c^{(m)} = m\pi$ and corresponds to $u(V) = V/2$. As shown in Figure A4, the domain of variation of u for this TE mode m

is $m\frac{\pi}{2} \leq u \leq (m+1)\frac{\pi}{2}$, while at the same time v goes from 0 with $n_{eff} = n_2$ (limit of no evanescence in the cladding i.e. confinement limit) to $(\pi/2)\sqrt{2m+1}$ with $n_{eff} = n_1$. We may define the normalized longitudinal propagation constant $b(V) = (n_{eff}^2 - n_2^2)/(n_1^2 - n_2^2)$ that takes values between 0 and 1 for a given mode, and can be seen as a confinement factor (fractional power in the core). For a given mode and when V increases, the mode effective index increases from the cladding index n_2 (the field extending then much in the cladding) to the core index n_1 (the field being then mostly confined in the core). An illustration for the fundamental mode is shown in Figure A4.

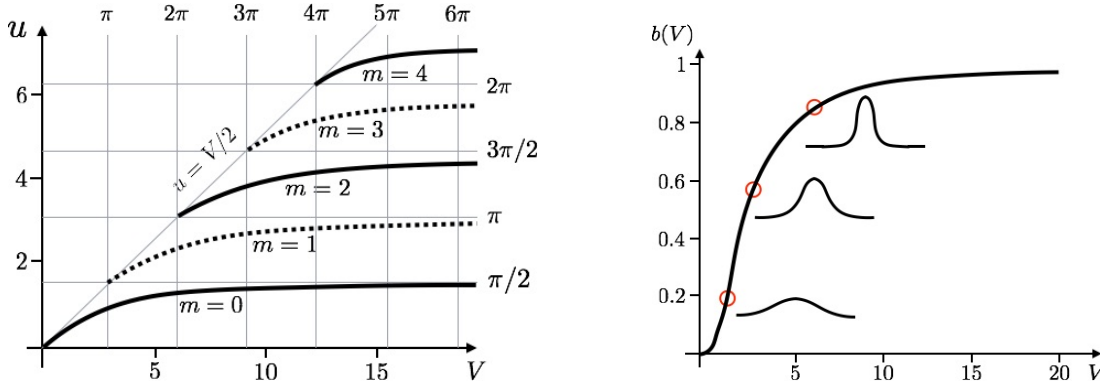


Figure A4. Solutions in the form $u(V)$ (left), and fundamental mode profiles with reduced propagation constant b as a function of the reduced frequency V (right).

The same procedure applies to describe the propagation of TM modes in a planar symmetric waveguide. The only differences lie in continuity conditions that enforce continuity of H_{0y} and $\frac{1}{n^2} \frac{dH_{0y}}{dx}$. These provide the following conditions for the existence of guided modes:

$$u \tan u = \left(\frac{n_1}{n_2}\right)^2 \sqrt{\left(\frac{V}{2}\right)^2 - u^2} \quad (\text{symmetric TM modes})$$

$$-u \cot u = \left(\frac{n_1}{n_2}\right)^2 \sqrt{\left(\frac{V}{2}\right)^2 - u^2} \quad (\text{antisymmetric TM modes})$$

This shows that cut-off frequencies are the same for TM and TE modes even though propagation constants are different, the planar waveguide being therefore birefringent.

Appendix A.2. Case of a step-index fiber waveguide

We now consider a circular, two-layer structure formed by an infinite cladding of constant refractive index n_2 surrounding a core of radius a and constant refractive index n_1 (Figure A1). The length is supposed infinite in the axial direction of propagation z , and we describe the optical guiding properties of such a structure in the case where the difference between n_1 and n_2 is small (weak guidance approximation). Placing in the cylindrical coordinate system, with invariance of the circular fiber along ϕ imposing

2π -periodicity (even though no invariance of functions along ϕ), electric and magnetic fields in the waveguide are respectively searched as:

$$\mathbf{E}(r, \phi, z, t) = \text{Re}\{\mathbf{E}_0(r, \phi)e^{j(\omega t - \beta z)}\} \quad ; \quad \mathbf{H}(r, \phi, z, t) = \text{Re}\{\mathbf{H}_0(r, \phi)e^{j(\omega t - \beta z)}\}$$

Maxwell's equations (A.1) then yield the following relations between fields components:

$$\begin{aligned} \beta E_{0\phi} - j \frac{1}{r} \frac{\partial E_{0z}}{\partial \phi} &= -\omega \mu_0 H_{0r} \quad ; \quad \beta E_{0r} - j \frac{\partial E_{0z}}{\partial r} = \omega \mu_0 H_{0\phi} \\ j \left(\frac{\partial E_{0\phi}}{\partial r} - \frac{1}{r} \frac{\partial E_{0r}}{\partial \phi} \right) &= \omega \mu_0 H_{0z} \quad ; \quad \beta H_{0\phi} - j \frac{1}{r} \frac{\partial H_{0z}}{\partial \phi} = \omega \epsilon_0 n^2 E_{0r} \\ \beta H_{0r} - j \frac{\partial H_{0z}}{\partial r} &= -\omega \epsilon_0 n^2 E_{0\phi} \quad ; \quad j \left(\frac{\partial H_{0\phi}}{\partial r} - \frac{1}{r} \frac{\partial H_{0r}}{\partial \phi} \right) = -\omega \epsilon_0 n^2 E_{0z} \end{aligned}$$

Similarly to the planar waveguide case, there might exist TE and TM modes when assuming circular symmetry i.e. field invariance along ϕ , but solutions with longitudinal components for both fields (called hybrid modes) also exist. The previous relations lead to two transverse vector propagation equations:

$$(\Delta_T + k_0^2 n^2 - \beta^2) \mathbf{E}_T = \mathbf{0} \quad ; \quad (\Delta_T + k_0^2 n^2 - \beta^2) \mathbf{H}_T = \mathbf{0}$$

and two longitudinal scalar propagation equations:

$$(\Delta_T + k_0^2 n^2 - \beta^2) E_z = 0 \quad ; \quad (\Delta_T + k_0^2 n^2 - \beta^2) H_z = 0$$

This has to be complemented with continuity conditions at the core/cladding interface. The first one is the continuity of tangential components of \mathbf{E} and \mathbf{H} . The second one is the continuity of normal components of \mathbf{D} and \mathbf{B} , that is the continuity of normal components of \mathbf{E} and \mathbf{H} in the weak guidance approximation; this results in the continuity of fields \mathbf{E} and \mathbf{H} . Additionally, the continuity of the longitudinal components E_z and H_z yields the continuity of the normal derivatives of these fields.

The transverse electric field may be written as

$$\mathbf{E}_T = \Psi(r, \phi) \mathbf{u}_T$$

with \mathbf{u}_T the unit transverse vector of arbitrary but constant direction (uniform polarization), leading to linearly polarized (LP) modes with two orthogonal polarization states for each ψ . This yields:

$$\frac{\partial^2 \Psi}{\partial r^2} + \frac{1}{r} \frac{\partial \Psi}{\partial r} + \frac{1}{r^2} \frac{\partial^2 \Psi}{\partial \phi^2} + [k_0^2 n^2 - \beta^2] \Psi = 0$$

We look for separable solutions $\Psi(r, \phi) = R(r)\Phi(\phi)$, that are products of radial and azimuthal variations, which results in:

$$\frac{r^2 d^2 R}{R dr^2} + \frac{r dR}{R dr} + r^2 [k_0^2 n^2 - \beta^2] = -\frac{1}{\Phi} \frac{d^2 \Phi}{d\phi^2} = \text{constant}$$

The function Φ being 2π -periodic, we write:

$$\frac{d^2 \Phi}{d\phi^2} + l^2 \Phi = 0$$

with l a positive integer. For $l = 0$, the only solution is $\Phi(\phi) = 1$, while for $l \geq 1$, there are two independent solutions $\Phi(\phi) = \cos(l\phi)$ and $\Phi(\phi) = \sin(l\phi)$.

Once l has been determined, radial variations of the transverse electric field satisfy:

$$\frac{r^2}{R} \frac{d^2 R}{dr^2} + \frac{r}{R} \frac{dR}{dr} + r^2 [k_0^2 n^2 - \beta^2] = l^2$$

As for the planar waveguide, the guidance condition reads $k_0 n_2 < \beta < k_0 n_1$, and we can introduce the transverse propagation coefficient $\alpha^2 = k_0^2 n_1^2 - \beta^2 > 0$ and extinction coefficient $\kappa^2 = \beta^2 - k_0^2 n_2^2 > 0$. We also define dimensionless (normalized) variables $u = \alpha a$ and $v = \kappa a$, and the reduced frequency $V = k_0 a \sqrt{n_1^2 - n_2^2}$ such that $u^2 + v^2 = V^2$. Two differential equations are then obtained:

$$r^2 \frac{d^2 R}{dr^2} + r \frac{dR}{dr} + (u^2 \frac{r^2}{a^2} - l^2) R = 0 \quad \text{in the core } (0 \leq r \leq a) \quad (\text{A.4})$$

$$r^2 \frac{d^2 R}{dr^2} + r \frac{dR}{dr} - (v^2 \frac{r^2}{a^2} + l^2) R = 0 \quad \text{in the cladding } (r \geq a) \quad (\text{A.5})$$

Solutions of (A.4), that describe the radial dependence of the guided modes inside the core, correspond to Bessel functions of the first kind J_l or the second kind Y_l (see Figure A5). Only the first set of solutions $R(r) = J_l(u \frac{r}{a})$, that behave as damped oscillations, is admissible; the other set $R(r) = Y_l(u \frac{r}{a})$ has no physical sense as it diverges at the core center ($r \rightarrow 0$).

Solutions of (A.5), that describe the radial dependence of the guided modes in the cladding, correspond to modified Bessel functions of the first kind I_l or the second kind K_l (see Figure A5). Only the second set of solutions $R(r) = K_l(v \frac{r}{a})$, that remain finite in the cladding and vanish when $r \rightarrow +\infty$ with asymptotic evolution in $\sqrt{\frac{\pi}{2r}} e^{-r}$, is admissible; the other set $R(r) = I_l(v \frac{r}{a})$ has no physical sense with unbounded cladding as it diverges when $r \rightarrow \infty$ with asymptotic evolution in $\sqrt{\frac{1}{2\pi r}} e^r$.

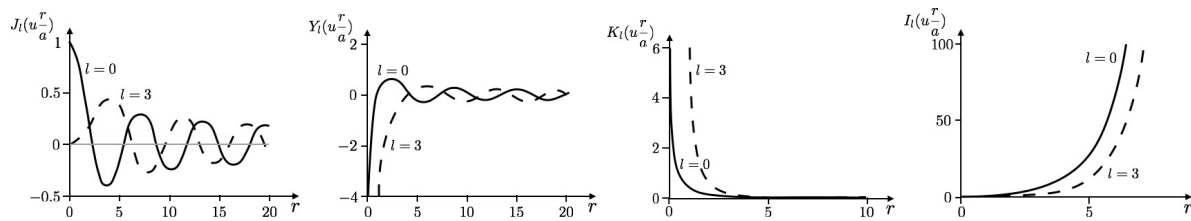


Figure A5. Bessel functions of the first and second kinds J_l and Y_l , and modified Bessel functions of the second and first kinds K_l and I_l , for $l = 0$ and $l = 3$.

Consequently, combining the azimuthal and radial parts and writing the continuity of $\Psi_l(r, \phi)$ at $r = a$, the general solutions for the whole fiber read:

$$\Psi_l(r, \phi) = A J_l(u \frac{r}{a}) \{ \cos(l\phi); \sin(l\phi) \} \quad \text{for } r < a$$

$$\Psi_l(r, \phi) = A \frac{J_l(u)}{K_l(v)} K_l(v \frac{r}{a}) \{ \cos(l\phi); \sin(l\phi) \} \quad \text{for } r > a$$

The continuity of the normal derivative of Ψ at $r = a$ introduces an additional condition:

$$u \frac{J'_l(u)}{J_l(u)} = v \frac{K'_l(v)}{K_l(v)} \implies u \frac{J_{l\pm 1}(u)}{J_l(u)} = \pm v \frac{K_{l\pm 1}(v)}{K_l(v)} \quad (\text{A.6})$$

where we used properties $\pm u J'_l(u) = l J_l(u) - u J_{l\pm 1}(u)$ and $\pm v K'_l(v) = l K_l(v) - \mp v K_{l\pm 1}(v)$. Equation (A.6) is the dispersion relation for the LP modes, defining the longitudinal propagation constant as a function of the normalized frequency V . Introducing again the normalized longitudinal propagation constant $b = \frac{(\beta^2/k_0^2) - n_2^2}{n_1^2 - n_2^2}$, with $u = V\sqrt{1-b}$ and $v = V\sqrt{b}$, the dispersion relation can be re-written as:

$$\sqrt{1-b} \frac{J_{l\pm 1}(V\sqrt{1-b})}{J_l(V\sqrt{1-b})} = \pm \sqrt{b} \frac{K_{l\pm 1}(V\sqrt{b})}{K_l(V\sqrt{b})}$$

For each value of l , the equation provides m possible discrete values for b , this number being a function of V . Each guided mode is referenced as LP_{lm} , and the associated effective index is:

$$n_{eff}(V) = \beta(V)/k_0 = \sqrt{n_2^2 + b(V).(n_1^2 - n_2^2)}$$

Figure A6 shows solutions for $u(V)$. We observe that for $V < 2.405$, the fundamental mode LP_{01} is the only mode to propagate; the fiber thus operates in the single mode regime. The number of guided modes supported by the fiber increases with increasing values of V . Cut-off frequencies, defined by $b(V) = 0$, may thus be calculated by solving $J_l(V) = 0$. In particular, the value $V = 2.405$ is the normalized cut-off frequency of the LP_{11} mode. Also, the radial repartitions of fundamental and third-order modes are given in Figure A6.

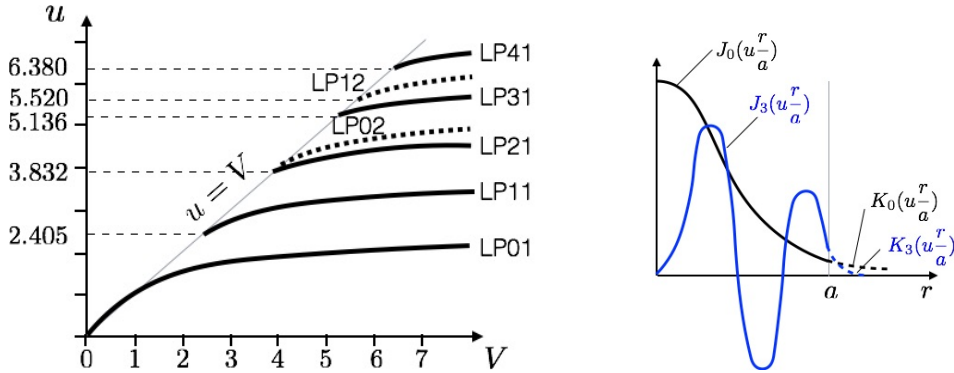


Figure A6. First LP_{lm} modes with functions $u(V)$ (left), and radial repartition for two modes of a step index fiber (right).

The variations of intensity of modes LP_{lm} are shown in Figure A7. They are characterized by:

- oscillations of Bessel functions with the value of r , within the core. The number of extrema of the oscillation with r is equal to m ;

- a periodicity in ϕ , defined by the first index l . A 2π rotation at constant r in the field goes through $2l$ cancellations of the amplitude, i.e. l dark radial fringes in the field. A maximum at the center of the core is specific to LP_{0m} modes;
- a monotonic decay of the amplitude in the cladding.

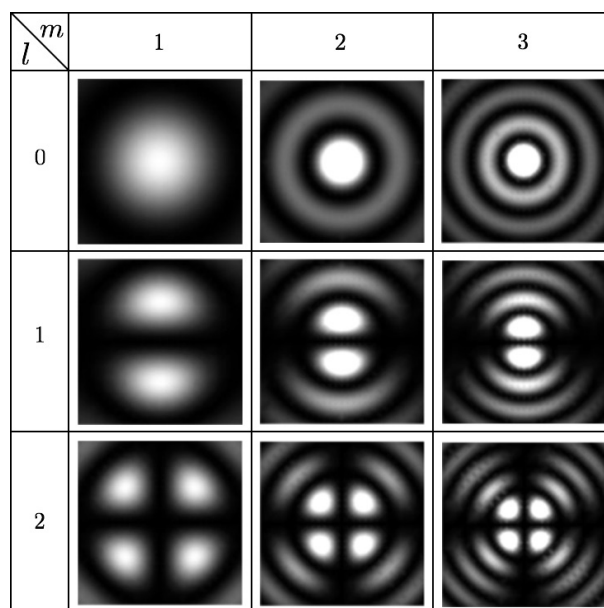


Figure A7. Intensity distributions of the LP_{lm} modes.

References

- [1] Agrawal G P 2002 *Fiber-optic communication systems* John Wiley & Sons, 3rd ed. New York
- [2] Agrawal G P 2007 *Nonlinear fiber optics* Academic Press, 4th ed. San Diego
- [3] Alahbabi M N, Cho Y T and Newson T P 2005 Simultaneous temperature and strain measurement with combined spontaneous Raman and Brillouin scattering *Optics Letters* **30** 1276-1278
- [4] Alan R 1999 Distributed optical-fibre sensing *Measurement Science and Technology* **10**(8) R75
- [5] Alj I, Quiertant M, Khadour A, Grando Q, Terrade B, Renaud J C and Benzarti K 2020 Experimental and numerical investigation on the strain response of distributed optical fiber sensors bonded to concrete: Influence of the adhesive stiffness on crack monitoring performance *Sensors* **20** 5788
- [6] Alwis L S M, Bremer K and Roth B 2021 Fiber optic sensors embedded in textile-reinforced concrete for smart structural health monitoring: a review *Sensors* **21** 4948
- [7] Ameduri S, Ciminello M, Dimino I, Concilio A, Catignani A and Mancinelli R 2019 Distributed sensor placement optimization for computer aided structural health monitoring *Archive of Mechanical Engineering* **66**(1) 111-1127
- [8] Antunes P, Lima H, Alberto N, Bilro L, Pinto P, Costa A, Rodrigues H, Pinto J L, Nogueira R, Varum H and André P S 2011 Optical sensors based on fiber Bragg gratings for structural health monitoring *New Developments in Sensing Technology for Structural Health Monitoring*, Springer 253-295
- [9] Aoyama K, Nakagawa K and Itoh T 1981 Optical time domain reflectometry in a single-mode fiber *IEEE Journal of Quantum Electronics* **17**(6) 862-868

- [10] Aulakh N, Chhabra J, Singh N and Jain S 2004 Microbend resolution enhancing technique for fiber optic based sensing and monitoring of landslides *Experimental Techniques* **28**(3) 37-42
- [11] Avci O, Abdeljaber O, Kiranyaz S, Hussein M, Gabbouj M, Inman D J 2021 A review of vibration-based damage detection in civil structures: from traditional methods to machine learning and deep learning applications *Mechanical Systems and Signal Processing* **147** 107077
- [12] Azam S E 2014 *Online damage detection in structural systems* Springer International Publishing
- [13] Badar M, Kobayashi H and Iwashita K 2016 Spatial resolution improvement in OFDR using four wave mixing and DSB-SC modulation *IEEE Photonics Technology Letters* **28**(15) 1680-1683
- [14] Bado M F, Casas J R, Dey A and Berrocal C G 2020 Distributed optical fiber sensing bonding techniques performance for embedment inside reinforced concrete structures *Sensors* **20** 5788
- [15] Bado M F and Casas J R 2021 A review of recent distributed optical fiber sensors applications for civil engineering structural health monitoring *Sensors* **21** 1818
- [16] Baker C, Lu Y, Song J 2014 Incoherent optical frequency domain reflectometry based on a Kerr phase-interrogator *Optics Express* **22**(13) 15370-15375
- [17] Bao X and Chen L 2011 Recent progress in Brillouin scattering based fiber sensors *Sensors* **11**(4) 4152-4187
- [18] Bao X and Chen L 2012 Recent progress in distributed fiber optic sensors *Sensors* **12**(7) 8601-8639
- [19] Bao Y, Tang F, Chen Y, Meng W, Huang Y and Chen G 2016 Concrete pavement monitoring with PPP-BOTDA distributed strain and crack sensors *Smart Structures and Systems* **18** 405-423
- [20] Bao X and Wang Y 2021 Recent advancements in Rayleigh scattering-based distributed fiber sensors *Advanced Devices & Instrumentation* **2021** 8696571
- [21] Barazanchy D, Martinez M, Rocha B and Yanishevsky M 2014 A hybrid structural health monitoring system for the detection and localization of damage in composite structures *Journal of Sensors* **2014** 1-10
- [22] Barbosa C, Costa N, Ferreira L A, Araujo F M, Varum H, Costa A, Fernandes C and Rodrigues H 2008 Weldable fibre Bragg grating sensors for steel bridge monitoring *Measurement Science and Technology* **19** 125305
- [23] Barnoski M K and Jensen S M 1976 Fiber waveguides: a novel technique for investigating attenuation characteristics *Applied Optics* **15**(9) 2112-2115
- [24] Barnoski M K, Rourke M D, Jensen S M and Melville R T 1977 Optical time domain reflectometer *Applied Optics* **16** 2375-2379
- [25] Barrias A, Casas J R and Villalba S 2016 A review of distributed optical fiber sensors for civil engineering applications *Sensors* **16**(5) 748
- [26] Barrias A, Casas J R and Villalba S 2018 Embedded distributed optical fiber sensors in reinforced concrete structures - A case study *Sensors* **18** 980
- [27] Barrias A, Casas J R and Villalba S 2019 SHM of reinforced concrete elements by Rayleigh Backscattering DOFS *Frontiers in Built Environment* **5** 30
- [28] Barrias A, Casas J R and Villalba S 2019 Distributed optical fibre sensors in concrete structures: Performance of bonding adhesives and influence of spatial resolution *Structural Control and Health Monitoring* **26** 1-16
- [29] Barton E N, Ogin S L, Thorne A M, Reed G T and Le Page B H 2001 Interaction between optical fibre sensors and matrix cracks in cross-ply GRP laminates - part 1: passive optical fibers *Composites Science and Technology* **61**(13) 1863-1869
- [30] Bernini R, Minardo A and Zeni L 2004 Stimulated Brillouin scattering frequency- domain analysis in a single-mode optical fiber for distributed sensing *Optics Letters* **29**(17) 1977-1979
- [31] Bernini R, Minardo A and Zeni L 2011 Distributed sensing at centimeter-scale spatial resolution by BOFDA: Measurements and signal processing *IEEE Photonics Journal* **4**(1) 48-56
- [32] Berrocal C G, Fernandez I and Rempling R 2021 Crack monitoring in reinforced concrete beams by distributed optical fiber sensors *Structure and Infrastructure Engineering* **17**(1) 124-139
- [33] Boldyreva E, Cotillard R, Laffont G, Ferdinand P, Cambet D, Jeannot J P, Charvet P, Albaladéjo S and Rodriguez G 2014 Distributed temperature monitoring for liquid sodium leakage detection

- using OFDR-based Rayleigh backscattering *Proceedings of SPIE, 23rd International Conference on Optical Fibre Sensors* 91576N
- [34] Bolognini G and Hartog A 2013 Raman-based fibre sensors: Trends and applications *Optical Fiber Technology* **19**(6) 678-688
- [35] Boyd R W 2008 *Nonlinear Optics* 3rd ed. New York, Academic Press
- [36] Broth Z and Hoult N A 2020 Dynamic distributed strain sensing to assess reinforced concrete behaviour *Engineering Structures* **204** 110036
- [37] Brown G A and Hartog A H 2002 Optical fiber sensors in upstream oil & gas *Journal of Petroleum Technology* **54** 63-65
- [38] Buck J A 2004 *Fundamentals of Optical Fibers* 2nd Edition
- [39] Cawley P 2018 Structural health monitoring: Closing the gap between research and industrial deployment *Structural Health Monitoring* **17**(5) 1225-1244
- [40] Cazzulani G, Chieppi M, Colombo A and Pennacchi P 2018 Optimal sensor placement for continuous optical fiber sensors *Proceedings SPIE, Sensors and Smart Structures Technologies for Civil, Mechanical, and Aerospace Systems* **10598** 1059844
- [41] Chamoin L 2021 DREAM-ON : Merging advanced sensing techniques and simulation tools for future structural health monitoring technologies *The Project Repository Journal* **10** 124-127
- [42] Chen T, Wang Q, Chen R, Zhang B, Chen K P, Maklad M and Swinehart P R 2012 Distributed hydrogen sensing using in-fiber Rayleigh scattering *Applied Physics Letters* **100**(19) 191105
- [43] Chesné S and Deraemaeker A 2013 Damage localization using transmissibility functions: a critical review *Mechanical Systems and Signal Processing* **38** 569-584
- [44] Chiao R, Townes C and Stoicheff B 1964 Stimulated Brillouin scattering and coherent generation of intense hypersonic waves *Physical Review Letters* **12**(21) 592
- [45] Chinesta F, Cueto E, Abisset-Chavanne E, Duval J.L and El Khaldi F 2020 Virtual, digital and hybrid twins: A new paradigm in data-based engineering and engineered data *Archives of Computational Methods in Engineering* **27**(1) 105-134
- [46] Chou T W, Gao L, Thostenson E T, Zhang Z and Byun J H 2010 An assessment of the science and technology of carbon nanotube-based fibers and composites *Composites Science and Technology* **70** 1-19
- [47] Claire D, Hild F and Roux S 2002 Identification of damage fields using kinematic measurements *Comptes-Rendus Mécanique* **330** 729-734
- [48] Corigliano A and Mariani S 2001 Parameter identification of a time-dependent elastic-damage interface model for the simulation of debonding in composites *Composites Science and Technology* **61**(2) 191-203
- [49] Culshaw B 2006 The optical fibre Sagnac interferometer: An overview of its principles and applications *Measurement Science and Technology* **17** R1-R16
- [50] Culshaw B and Kersey A 2008 Fiber-optic sensing: A historical perspective *Journal of Lightwave Technology* **26**(9) 1064-1078
- [51] Dakin J, Pratt D, Bibby G and Ross J 1985 Distributed optical fibre Raman temperature sensor using a semiconductor light source and detector *Electronics Letters* **21**(13) 569-570
- [52] Dammig M, Zinner G, Mitschke F and Welling H 1993 Stimulated Brillouin-scattering in fibers with and without external feedback *Physical Review A* **48**(4) 3301-3309
- [53] Darema F 2004 Dynamic data driven application systems: a new paradigm for application simulations and measurements *Lecture Notes in Computer Science* **3038** 662-669
- [54] Darema F 2015 DDDAS, a key driver for large-scale-big-sata and large-scale-big-computing *In S. Koziel, L. Leifsson, M. Lees, V.V Krzhizhanovskaya, J. Dongarra, P.M.A Sloot editors, ICCS 2015, Procedia Computer Science* **51** 2463
- [55] Davis C, Tejedor S, Grabovac I, Kopczyk J and Nuyens T 2012 High strain Fiber Bragg Gratings for structural fatigue testing of military aircraft *Photonics Sensors* **2**(3) 215-224
- [56] Di Sante R 2015 Fiber optic sensors for structural health monitoring of aircraft composite structures: Recent advances and applications *Sensors* **15** 18666-18713

- [57] Ding Z, Yao X S, Liu T, Du Y, Liu K, Han Q, Meng Z, Jiang J and Chen H 2013 Long measurement range OFDR beyond laser coherence length *IEEE Photonics Technology Letters* **25** 202-205
- [58] Ding Z, Yang D, Du Y, Liu K, Zhou Y, Zhang R, Xu Z, Jiang J and Liu T 2016 Distributed strain and temperature discrimination using two types of fiber in OFDR *IEEE Photonics Journal* **8** 6804608
- [59] Ding Z, Wang C, Liu K, Jiang J, Yang D, Pan G, Pu Z and Liu T 2018 Distributed optical fiber sensors based on optical frequency domain reflectometry: a review *Sensors* **18**(4) 1072
- [60] Doebbling S W, Farrar C R and Prime M B 1998 A summary review of vibration-based damage identification methods *Shock & Vibration Digest* **30**(2) 91-105
- [61] Dong Y, Chen L and Bao X 2010 High-spatial-resolution time-domain simultaneous strain and temperature sensor using Brillouin scattering and birefringence in a polarization-maintaining fiber *IEEE Photonics Technology Letters* **22**(18) 1364-1366
- [62] Dong X, Wang A, Zhang J, Han H, Zhao T, Liu X and Wang Y 2012 Combined attenuation and high-resolution fault measurements using chaos-OTDR *IEEE Photonics* **7**(6)
- [63] Du Y, Liu T, Ding Z and Feng B 2014 Method for improving spatial resolution and amplitude by optimized skew filter in long-range OFDR *IEEE Photonics Journal* **6**(5) 7802811
- [64] Du C, Dutta S, Kurup P, Yu T and Wang X 2020 A review of railway infrastructure monitoring using fiber optic sensors *Sensors and Actuators A: Physical* **303** 11728
- [65] Eaton N C, Drew R C and Geiger H 1995 Finite element stress and strain analysis in composites with embedded optical fiber sensors *Smart Materials and Structures* **4**(2) 113
- [66] Eickhoff W and Ulrich R 1981 Optical frequency domain reflectometry in single-mode fiber *Applied Physics Letters* **39**(9) 693-695
- [67] Eraerds P, Legré M, Zhang J, Zbinden H and Gisin N 2010 Photon counting OTDR: Advantages and limitations *Journal of Lightwave Technology* **28**(6) 952-964
- [68] Fan X, Koshikiya Y and Ito F 2009 Phase noise compensated optical frequency domain reflectometry *IEEE Journal of Quantum Electronics* **45**(6) 594-602
- [69] Fan W and Qiao P 2010 Vibration-based damage identification methods: a review and comparative study *Structural Health Monitoring* **9**(3) 83-111
- [70] Fang X, Luo H and Tang J 2005 Structural damage detection using neural network with learning rate improvement *Computers & Structures* **83**(25-26) 2150-2161
- [71] Fang Z, Chin K, Qu R and Cai H 2012 *Fundamentals of Optical Fiber Sensors* Wiley
- [72] Farrar C R and Worden K 2007 An introduction to structural health monitoring *Philosophical Transactions of the Royal Society A, Mathematical, Physical & Engineering Sciences* **365** 303-315
- [73] Farries M and Rogers A 1984 Distributed sensing using stimulated Raman interaction in a monomode optical fibre *Proceedings of SPIE- The International Society for Optical Engineering* **514** 121-132
- [74] Ferdinand P 2014 The evolution of optical fiber sensors technologies during the 35 last years and their applications in structure health monitoring *Proceedings of the 7th European Workshop on Structure Health Monitoring (EWSHM), Nantes, France*
- [75] Francis T S and Yin S 2002 *Fiber Optic Sensors* Marcel Dekker Inc.: New York, NY, USA
- [76] Friswell M I 2007 Damage identification using inverse methods *Philosophical Transactions of the Royal Society A: Mathematical, Physical and Engineering Sciences* **365**(1851) 393-410
- [77] Froggatt M and Moore J 1998 High-spatial-resolution distributed strain measurement in optical fiber with Rayleigh scatter *Applied Optics* **37**(10) 1735-1740
- [78] Froggatt M E 2009 Distributed strain and temperature discrimination in polarization maintaining fiber *U.S. Patent 7,538,883 B2, 26 May*
- [79] Galindez-Jamioy C A and Lopez-Higuera J M 2012 Brillouin distributed fiber sensors: an overview and applications *Journal of Sensors* **2012** 204121
- [80] Garus D, Krebber K, Schliep F and Golgolla T 1996 Distributed sensing technique based on Brillouin optical-fiber frequency-domain analysis *Optics Letters* **21**(17) 1402-1404

- [81] Gifford D K, Kreger S T, Sang A K, Froggatt M E, Duncan R G, Wolfe M S and Soller B J 2007 Swept-wavelength interferometric interrogation of fiber Rayleigh scatter for distributed sensing applications *Proceedings SPIE* 6770
- [82] Glisic B and Inaudi D 2007 *Fibre optic methods for structural health monitoring* John Wiley & Sons, Chichester, UK
- [83] Goshal A, Ayers J, Gurvich M, Urban M and Bordick N 2015 Experimental investigations in embedded sensing of composite components in aerospace vehicles *Composites Part B* **71** 52-62
- [84] Grattan K T V and Sun T Y 2000 Fiber optic sensor technology: an overview *Sensors and Actuators A Physical* **82** 40-61
- [85] Grave J H L, Haheim M L and Echtermeyer A T 2015 Measuring changing strain fields in composites with Distributed Fiber-Optic Sensing using the optical backscatter reflectometer *Composites Part B: Engineering* **74** 138-146
- [86] Guemes A, Fernandez-Lopez A and Soller B 2010 Optical fiber distributed sensing-Physical principles and applications *Structural Health Monitoring* **9**(3) 233-245
- [87] Guemes A, Fernandez-Lopez A and Fernandez P 2014 Damage detection in composite structures from fibre optic distributed strain measurements *Proceedings of the 7th European Workshop on Structural Health Monitoring, Nantes, France*
- [88] Guemes A 2014 Fiber Optic Strain Sensors *NATO-STO Lecture Series, STO-EN-AVT-220-03* 1-16
- [89] Guemes A, Fernandez-Lopez A, Diaz-Maroto P F, Lozano A, Sierra-Perez J 2018 Structural health monitoring in composite structures by fiber-optic sensors *Sensors* **18** 1094
- [90] Guo H, Xiao G, Mrad N and Yao J 2011 Fiber optic sensors for structural health monitoring of air platforms *Sensors* **11** 3687-3705
- [91] Guzman De Vitoria R, Yamamoto N, Miravete A and Wardle B L 2011 Multi-physics damage sensing in nano-engineered structural composites *Nanotechnology* **22** 185502
- [92] Habel W R and Krebber K 2011 Fiber-optic sensor applications in civil and geotechnical engineering *Photonic Sensors* **1** 268-280
- [93] Hartog A 1983 A distributed temperature sensor based on liquid-core optical fibers *Journal of Lightwave Technology* **1**(3) 498-509
- [94] Hartog A, Gold M 1984 On the theory of backscattering in single-mode optical fibers *Journal of Lightwave Technology* **2**(2) 76-82
- [95] Hartog A, Leach A P, Gold M P 1985 Distributed temperature sensors in solid-core fibers *Electronics Letters* **21-23** 1061-1062
- [96] Hartog A H 2017 *An Introduction to Distributed Optical Fiber Sensors* CRC Press
- [97] Hasegawa T and Hotate K 1999 Measurement of Brillouin gain spectrum distribution along an optical fiber by direct frequency modulation of a laser diode *Proceedings of SPIE* **3860** 306-316
- [98] Healey P and Hensel P 1980 Optical time domain reflectometry by photon counting *Electronics Letters* **16**(16) 631-633
- [99] Healey P 1986 Instrumentation principles for optical time domain reflectometry *Journal of Physics E: Scientific Instruments* **19**(5) 334
- [100] Hecht J 1999 *City of Light: the Story of Fiber Optics* OUP, USA
- [101] Hecht J 2006 *Understanding Fiber Optics* Prentice Hall, 5th Edition, USA
- [102] Heeder N, Shukla A, Chalivendra V and Yang S 2012 Sensitivity and dynamic electrical response of cnt-reinforced nanocomposites *Journal of Materials Science* **47**(8) 3808-3816
- [103] Hehr A, Norfolk M, Sheridan J, David M, Leser W, Leser P and Newman J A 2019 Spatial strain sensing using embedded fiber optics *Additive Manufacturing of Composites and Complex Materials, The Minerals, Metals & Materials Society* **71**(4) 1528-1534
- [104] Heiman D, Hamilton D S and Hellwarth R W 1979 Brillouin scattering measurements on optical glasses *Physical Review B* **19**(12) 6583-6592
- [105] Heinze S and Echtermeyer A T 2018 In-situ strain measurements in large volumes of hardening epoxy using Optical Backscatter Reflectometry *Applied Sciences* **8**(7) 1141
- [106] Hénault J M, Quiertant M, Delepine-Lesoille S, Salin J, Moreau G, Taillade F and Benzarti

- K 2012 Quantitative strain measurement and crack detection in RC structures using a truly distributed fiber optic sensing system *Construction and Building Materials* **37** 916-923
- [107] Hild F and Roux S 2012 Digital image correlation in *Optical Methods for Solid Mechanics - A Full-Field Approach*, Wiley 183-228
- [108] Hill KO and Meltz G 1997 Fiber Bragg grating technology fundamentals and overview *Journal of Lightwave Technology* **15** 1263-1276
- [109] Horiguchi T and Tateda M 1989 BOTDA-nondestructive measurement of single-mode optical fiber attenuation characteristics using Brillouin interaction: theory *Journal of Lightwave Technology* **7**(8) 1170-1176
- [110] Horiguchi T, Shimizu K, Kurashima T, Tateda M and Koyamada Y 1995 Development of a distributed sensing technique using Brillouin scattering *Journal of Lightwave Technology* **13**(7) 1296-1302
- [111] Hotate K and Hasegawa T 2000 Measurement of Brillouin gain spectrum distribution along an optical fiber with a high spatial resolution using a correlation-based technique - Proposal, experiment and simulation *IEICE Transactions on Electronics* **E83-C**(3) 405-411
- [112] Inaudi D and Glisic B 2005 Application of distributed fiber optic sensory for SHM *2nd International Conference on Structural Health Monitoring of Intelligent Infrastructure, Shenzhen, China*
- [113] Iribas H, Loayssa A, Sauser F, Llera M and Le Floch S 2017 Cyclic coding for Brillouin optical time-domain analyzers using probe dithering *Optics Express* **25** 8787-8800
- [114] Ito F, Fan X and Koshikiya Y 2012 Long-range coherent OFDR with light source phase noise compensation *Journal of Lightwave Technology* **30**(8) 1015-1024
- [115] Jones M 1993 Using simplex codes to improve OTDR sensitivity *IEEE Photonics Technology Letters* **5**(7) 822-824
- [116] Juarez J C and Taylor H F 2005 Polarization discrimination in a phase-sensitive optical time-domain reflectometer intrusion-sensor system *Optics Letters* **30** 3284-3286
- [117] Kania J K, Sorensen K K and Fellenius B H 2020 Application of distributed fibre optic sensing in piles *Geotechnical Engineering Journal of the SEAGS & AGSSEA* **51**(1) 94-102
- [118] Kashyap R 1999 *Fiber Bragg gratings* Optics and Photonics, Academic Press
- [119] Kee H H, Lees G P and Newson T P 2000 All-fiber system for simultaneous interrogation of distributed strain and temperature sensing by spontaneous Brillouin scattering *Optics Letters* **25**(10) 695-697
- [120] Keiser G 1991 *Optical Fiber Communications* McGraw-Hill International Editions
- [121] Khadour A 2018 *Capteurs distribués à fibres optiques: aspects physiques, développement et applications* HDR Univ. Paris-Est
- [122] Khan A, Ko D K, Lim S C and Kim H S 2019 Structural vibration-based classification and prediction of delamination in smart composite laminates using deep learning neural network *Composites Part B-Engineering* **161** 586-594
- [123] Kim B Y and Choi S S 1981 Backscattering measurement of bending-induced birefringence in single mode fibres *Electronics Letters* **17**(5) 193-194
- [124] Kinet D, Mégret P, Goossen K W, Qiu L, Heider D and Caucheteur C 2014 Fiber Bragg grating sensors toward structural health monitoring in composite materials: challenges and solutions *Sensors* **14**(4) 7394-7419
- [125] King J, Smith D, Richards K, Timson P, Epworth R and Wright S 1987 Development of a coherent OTDR instrument *Journal of Lightwave Technology* **5**(4) 616-624
- [126] Kingsley S A 1985 Fiber-optic sensors: Opportunities for distributed measurement *InTech* **32**(8) 44-48
- [127] Kingsley S A and Davies D E N 1985 OFDR diagnostics for fibre and integrated-optic systems *Electronics Letters* **21**(10) 434-435
- [128] Kishida K, Yamauchi Y and Guzik A 2014 Study of optical fibers strain-temperature sensitivities using hybrid Brillouin-Rayleigh System *Photonic Sensors* **4**(1) 1-11

- [129] Klar A, Dromy I and Linker R 2014 Monitoring tunneling induced ground displacements using distributed fiber-optic sensing *Tunnelling and Underground Space Technology* **40** 141-50
- [130] Koyamada Y, Imahama M, Kubota K and Hogari K 2009 Fiber-optic distributed strain and temperature sensing with very high measure and resolution over long range using coherent OTDR *Journal of Lightwave Technology* **27**(9) 1142-1146
- [131] Krohn D A, MacDougall W and Mendez A 2015 *Fiber Optic Sensors: Fundamentals and Applications* SPIE Press, 4th edition
- [132] Kung A, Budin J, Thevenaz L and Robert P 1997 Rayleigh fiber optics gyroscope *IEEE Photonics Technology Letters* **9**(7) 973-975
- [133] Kurashima T, Horiguchi T and Tateda M 1990 Distributed-temperature sensing using stimulated Brillouin scattering in optical silica fibers *Optics Letters* **15**(18) 1038-1040
- [134] Kurashima T, Horiguchi T, Izumita H, Furukawa S and Koyamada Y 1993 Brillouin optical-fiber time domain reflectometry *IEICE Transactions on Communications* **76**(4) 382-390
- [135] Lecoeuche V, Webb D J, Pannell CN and Jackson D A 2000 Transient response in high-resolution Brillouin-based distributed sensing using probe pulses shorter than the acoustic relaxation time *Optics Letters* **25** 156-158
- [136] Lee D, Yoon H, Kim P, Park J, Kim N Y and Park N 2005 SNR enhancement of OTDR using biorthogonal codes and generalized inverses *IEEE Photonics Technology Letters* **17**(1) 163-165
- [137] Lee D, Yoon H, Kim P, Park J and Park N 2006 Optimization of SNR improvement in the noncoherent OTDR based on simplex codes *Journal of Lightwave Technology* **24** 322-328
- [138] Lee B H, Kim Y H, Park K S, Eom J B, Kim M J, Rho B S and Choi H Y 2012 Interferometric fiber optic sensors *Sensors* **12** 2467-2486
- [139] Leung C K Y, Wan K T, Inaudi D, Bao X, Habel W, Zhou Z, Ou J, Ghandehari M, Wu H C and Imai M 2013 Review: Optical fiber sensors for civil engineering applications *Materials and Structures* **48** 871-906
- [140] Li W, Bao X, Li Y and Chen L 2008 Differential pulse-width pair BOTDA for high spatial resolution sensing *Optics Express* **16** 21616-21625
- [141] Li J, Kapania R K and Spillman W B 2008 Placement optimization of distributed-sensing fiber-optic sensors using genetic algorithms *AIAA Journal* **46**(4) 824-836
- [142] Li W, Chen L and Bao X 2013 Compensation of temperature and strain coefficients due to local birefringence using optical frequency domain reflectometry *Optics Communications* **311** 26-32
- [143] Li D, Ho S C M, Song G, Ren L and Li H 2015 A review of damage detection methods for wind turbine blades *Smart Materials and Structures* **24** 33001-33025
- [144] Liang H, Li W, Linze N, Chen L and Bao X 2010 High-resolution DPP-BOTDA over 50 km LEAF using return-to-zero coded pulses *Optics Letters* **35** 1503-1505
- [145] Liehr S, Nother N and Krebber K 2010 Incoherent optical frequency domain reflectometry and distributed strain detection in polymer optical fibers *Measurement Science and Technology* **21**(1)
- [146] Liehr S, Munzenberger S and Krebber K 2018 Wavelength-scanning coherent OTDR for dynamic high strain resolution sensing *Optics Express* **26**(8) 10573-10588
- [147] Liu X, Escamilla-Ambrosio P J and Lieven N A J 2009 Extended Kalman filtering for the detection of damage in linear mechanical structures *Journal of Sound & Vibration* **325**(4-5) 1023-1046
- [148] Lopatin C 2018 Aerospace applications of optical fiber mechanical sensors *Opto-Mechanical Fiber Optic Sensors* 237-162
- [149] Lopez-Higuera J M 2002 *Handbook of optical fibre sensing technology* Wiley
- [150] Lopez-Higuera J M, Cobo L R, Incera A Q and Cobo A 2011 Fiber optic sensors in structural health monitoring *Journal of Lightwave Technology* **29**(4) 587-608
- [151] Lu Y, Zhu T, Chen L and Bao X 2010 Distributed vibration sensor based on coherent detection of phase-OTDR *Journal of Lightwave Technology* **28**(22) 3243-3249
- [152] Lu X, Soto M A and Thévenaz L 2017 Temperature-strain discrimination in distributed optical fiber sensing using phase-sensitive optical time-domain reflectometry *Optics Express* **25**(14) 16059-16071

- [153] Lu P, Lalam N, Badar M, Liu B, Chorpene B T, Buric M P, Ohodnicki R 2019 Distributed optical fiber sensing: review and perspective *Applied Physics Review* **6** 041302
- [154] <http://lunainc.com>
- [155] Majumder M, Gangopadhyay T K, Chakraborty A K, Dasgupta K and Bhattacharya D K 2008 Fibre Bragg gratings in structural health monitoring-Present status and applications *Sensors and Actuators A: Physical* **147**(1) 150-164
- [156] Distributed Fiber Optic Sensor Market, available online: <https://www.psmarketresearch.com/market-analysis/distributed-fiber-optic-sensor-market>
- [157] Martinez Bueno P, Martinez M J, Rans C D and Benedictus R 2016 Strain monitoring using a Rayleigh backscattering system for a composite UAV wing instrumented with an embedded optical fiber *Advanced Materials Research* **1135** 1-19
- [158] Massa J S, Buller G S, Walker A C, Cova S, Umasuthan M and Wallace A M 1998 Time-of-flight optical ranging system based on time-correlated single-photon counting *Applied Optics* **37**(31) 7298-7304
- [159] Masoudi A, Belal M and Newson T 2013 A distributed optical fibre dynamic strain sensor based on phase-OTDR *Measurement Science and Technology* **24**(8) 085204
- [160] Mata-Falcon J, Haefliger S, Lee M, Galkovski T and Gehri N 2020 Combined application of distributed fibre optical and digital image correlation measurements to structural concrete experiments *Engineering Structures* **225** 111309
- [161] Maurin L, Ferdinand P, Nony F and Villalonga S 2014 OFDR distributed strain measurements for SHM of hydrostatic stressed structures: An application to high pressure hydrogen storage type IV composite vessels - H2E project *EWSHM - 7th European Workshop on Structural Health Monitoring, Nantes*
- [162] McCormick N and Lord J 2010 Digital image correlation *Materials Today* **13** 52-54
- [163] Minakuchi S and Takeda N 2013 Recent advancement in optical fiber sensing for aerospace composite structures *Photonic Sensors* **3** 345-354
- [164] Minardo A, Bernini R, Ruiz-Lombera R, Mirapeix J, Lopez-Higuera J M and Zeni L 2016 Proposal of Brillouin optical frequency-domain reflectometry (BOFDR) *Optics Express* **24**(26) 29994-30001
- [165] Mohamad H, Soga K, Bennett P J, Mair R J and Lim C S 2011 Monitoring twin tunnel interaction using distributed optical fiber strain measurements *Journal of Geotechnical and Geoenvironmental Engineering* **138**(8) 957-967
- [166] Moore E D and McLeod R R 2008 Correction of sampling errors due to laser tuning rate fluctuations in swept-wavelength interferometry *Optics Express* **16** 13139-13149
- [167] Motil A, Bergman A and Tur M 2015 State of the art of Brillouin fiber-optic distributed sensing *Optics & Laser Technology* **78** 1-23
- [168] Muanenda Y, Taki M and Di Pasquale F 2014 Long-range accelerated BOTDA sensor using adaptive linear prediction and cyclic coding *Optics Letters* **39** 5411-5414
- [169] Nakayama J, Iizuka K and Nielsen J 1987 Optical fiber fault locator by the step frequency method *Applied Optics* **26**(3) 440-443
- [170] Nakazawa M 1983 Rayleigh backscattering theory for single-mode optical fibers *Journal of the Optical Society of America* **73**(9) 1175-1180
- [171] Niklès M, Thévenaz L and Robert A 1997 Brillouin gain spectrum characterization in single-mode optical fibers *Journal of Lightwave Technology* **15**(10) 1842-1851
- [172] Oberson P, Huttner B and Gisin N 1999 Frequency modulation via the Doppler effect in optical fibers *Optics Letters* **24**(7) 451-453
- [173] Ohashi M, Shiraki K and Tajima K 1992 Optical loss property of silica-based single-mode fibers *Journal of Lightwave Technology* **10**(5) 539-543
- [174] Ohno S, Iida D, Toge K and Manabe T 2016 Long-range measurement of Rayleigh scatter signature beyond laser coherence length based on coherent optical frequency domain reflectometry *Optics Express* **24**(17) 19651

- [175] Othonos A and Kalli K 1999 *Fiber Bragg Gratings: Fundamentals and Applications in Telecommunications and Sensing* Artech House
- [176] Palmieri L and Schenato L 2013 Distributed optical fiber sensing based on Rayleigh scattering *Open Optics Journal* **7**(11) 104-127
- [177] Panopoulou A, Roulias D, Loutas T H and Kostopoulous V 2012 Health monitoring of aerospace structures using fibre Bragg Gratings combined with advanced signal processing and pattern recognition techniques *Strain* **48** 267-277
- [178] Parker T R, Farhadiroushan M, Handerek V, Rogers A 1997 A fully distributed simultaneous strain and temperature sensor using spontaneous Brillouin backscattering *IEEE Photonics Technology Letters* **9**(7) 979-981
- [179] Passy R, Gisin N and von der Weid J P 1995 High-sensitivity-coherent optical frequency domain reflectometry for characterization of fiber-optic network components *Photonics Technology Letters, IEEE* **7**(6) 667-669
- [180] Pastor-Graells J, Martins H F, Garcia-Ruiz A, Martin-Lopez S and Gonzalez-Herraez M 2016 Single-shot distributed temperature and strain tracking using direct detection phase-sensitive OTDR with chirped pulses *Optics Express* **24**(12) 13121-13133
- [181] Petermann K 1976 Microbending loss in monomode fibres *Electronics Letters* **12**(4) 107-109
- [182] Posey J R, Johnson G and Vohra S 2000 Strain sensing based on coherent Rayleigh scattering in an optical fibre *Electronics Letters* **36**(20) 1688-1689
- [183] Pradhan H S and Sahu P K 2015 Characterisation of Raman distributed temperature sensor using deconvolution algorithms *IET Optoelectronics* **9**(2) 101-107
- [184] Propst A, Peters K, Zikry M A, Schultz S, Kunzler W, Zhu Z, Wirthlin M and Selfridge R 2010 Assessment of damage in composite laminates through dynamic, full-spectral interrogation of fiber Bragg grating sensors *Smart Materials and Structures* **19**
- [185] Prudencio E, Bauman P, Williams S, Faghihi D, Ravi-Chandar K and Oden J T 2014 Real-time inference of stochastic damage in composite materials *Composites Part B: Engineering* **67** 209-219
- [186] Rahim N A A, Kutz J J, White M M, Michel J, Sang A K, Froggatt M E, Klute S M and Gifford D K 2013 Dynamic monitoring of fan blade using high resolution, distributed fiber optic sensing *Proceedings of the SAMPE Technical Conference, Wichita, KS, USA*
- [187] Rajan G and Prusty B G 2016 *Structural health monitoring of composite structures using fiber optic methods* CRC Press
- [188] Rajeev P, Kodikara J, Chiu W K and Kuen T 2013 Distributed optical fiber sensors and their applications in pipelines monitoring *Key Engineering Materials* **558** 424-434
- [189] Ramakrishnan M, Rajan G, Semenova Y and Farrell G 2016 Overview of fiber optic sensor technologies for strain/temperature sensing applications in composite materials *Sensors* **16**(1) 99
- [190] Raman C V and Krishnan K S 1928 A new type of secondary radiation *Nature* **121** 501-502
- [191] Rao Y J, Luo J, Ran Z L, Yue J F, Luo X D and Zhou Z 2009 Long-distance fiber-optic ϕ -OTDR intrusion sensing system *Proceedings of SPIE - The International Society for Optical Engineering* **7503**
- [192] Ravet F, Briffod F, Glisc B, Nikles M and Inaudi D 2009 Submillimeter crack detection with Brillouin-based fiber-optic sensors *IEEE Sensors Journal* **9** 1391-1396
- [193] Rhim J and Lee S W 1995 A neural network approach for damage detection and identification of structures *Computational Mechanics* **16**(6) 437-443
- [194] Rodriguez G, Casas J R, Villalba S 2015 SHM by DOFS in civil engineering: A review *Structural Monitoring and Maintenance* **2**(4) 357-382
- [195] Rodriguez G, Casas J R, Villalba S 2015 Cracking assessment in concrete structures by distributed optical fiber *Smart Materials and Structures* **24** 035005
- [196] Rodriguez G, Casas J R, Villalba S 2019 Shear crack width assessment in concrete structures by 2D distributed optical fiber *Engineering Structures* **195** 508-523

- [197] Rogers A J 1980 Polarisation optical time domain reflectometry *Electronics Letters* **16**(13) 489-490
- [198] Rogers A 1988 Distributed optical-fibre sensors for the measurement of pressure, strain and temperature *Physics Reports* **169**(2) 99-143
- [199] Rogers A 1999 Distributed optical-fibre sensing *Measurement Science and Technology* **10**(8) 75-99
- [200] Rosafalco L, Torzoni M, Manzoni A, Mariani S and Corigliano A 2021 Online structural health monitoring by model order reduction and deep learning algorithms *Computers & Structures* **255** 106604
- [201] Rouchier S, Foray G, Godin N, Woloszyn M and Roux J J 2013 Damage monitoring in fibre reinforced mortar by combined digital image correlation and acoustic emission *Construction and Building Materials* **38** 371-380
- [202] Saeedifar M and Zarouchas D 2020 Damage characterization of laminated composites using acoustic emission: A review *Composites Part B-Engineering* **195** 108039
- [203] Saeter E, Lasn K, Nony F and Echtermeyer A T 2019 Embedded optical fibres for monitoring pressurization and impact of filament wound cylinders *Composite Structures* **210** 608-617
- [204] Saleh B E A and Teich M C 2019 *Fundamentals of Photonics* Wiley-VCH
- [205] Samiec D 2012 Distributed fibre-optic temperature and strain measurement with extremely high spatial resolution *Photonik International* **1** 10-13
- [206] Sanborn E E, Sang A K, Wesson E, Wigent D E and Lucier G 2011 Distributed fiber optic strain measurement using Rayleigh scatter in composites structures *Experimental and Applied Mechanics* **6** 461-470
- [207] Schwartz M 2008 *Encyclopedia of smart materials*
- [208] Schenato L 2017 A review of distributed fibre optic sensors for geo-hydrological applications *Applied Sciences* **7** 896
- [209] Shelby R M, Levenson M D and Bayer P W 1985 Guided acoustic-wave Brillouin scattering *Physical Review B: Condensed Matter* **31**(8) 5244-5252
- [210] Shen S, Wu Z, Yang C, Wan C, Tang Y and Wu G 2010 An improved conjugated beam method for deformation monitoring with a distributed sensitive fiber optic sensor *Structural Health Monitoring* **9**(4) 361-378
- [211] Shibata N, Waarts R G and Braun R P 1987 Brillouin-gain spectra for single-mode fibers having pure-silica, GeO₂-doped, and P₂O₅-doped cores *Optics Letters* **12** 269-271
- [212] Shimizu K, Horiguchi T and Koyamada Y 1992 Characteristics and reduction of coherent fading noise in Rayleigh backscattering measurement for optical fibers and components *Journal of Lightwave Technology* **10**(7) 982-987
- [213] Shimizu K, Horiguchi T, Koyamada Y and Kurashima T 1993 Coherent self-heterodyne detection of spontaneously Brillouin-scattered light waves in a single-mode fiber *Optics Letters* **18**(3) 185-187
- [214] Shivakumar K and Emmanwori L 2004 Mechanics of failure of composite laminates with an embedded fiber optic sensor *Journal of Composite Materials* **38** 669-680
- [215] Sierra-Pérez J, Guemes A and Mujica L E 2013 Damage detection by using FBGs and strain field pattern recognition techniques *Smart Materials and Structures* **22** 25011
- [216] Sierra-Pérez J, Torres-Arredondo M A and Guemes A 2016 Damage and nonlinearities detection in wind turbine blades based on strain field pattern recognition. FBGs, OBR and strain gauges comparison *Composite Structures* **135** 156-166
- [217] Siivola J, Minakuchi S, Mizutani T and Takeda N 2015 Evaluation of damage detectability in practical sandwich structure application conditions using distributed fiber optic sensor *Composites Structural Health Monitoring* **15**(1)
- [218] Snyder A W and Love J D 1983 *Optical Waveguide Theory* Chapman and Hall
- [219] Soga K and Luo L 2018 Distributed fiber optics sensors for civil engineering infrastructure sensing *Journal of Structural Integrity and Maintenance* **3** 1-21
- [220] Sohn H, Farrar C R, Hemez F M and Czarnecki J J 2002 A review of structural health monitoring

- literature 1996-2001 *Los Alamos National Laboratory: Los Alamos, NM, USA*
- [221] Soller B, Gifford D, Wolfe M and Froggatt M C 2005 High resolution optical frequency domain reflectometry characterization of components and assemblies *Optics Express* **13**(2) 666-674
- [222] Song K Y, He Z and Hotate K 2006 Distributed strain measurement with millimeter-order spatial resolution based on Brillouin optical correlation domain analysis *Optics Letters* **31**(17) 2526-2528
- [223] Song J, Li W, Lu P, Xu Y, Chen L and Bao X 2014 Long-range high spatial resolution distributed temperature and strain sensing based on optical frequency-domain reflectometry *IEEE Photonics Journal* **6**(3) 6801408
- [224] Takada K, Himeno A and Yukimatsu K 1991 Phase-noise and shot-noise limited operations of low coherence optical time domain reflectometry *Applied Physics Letters* **59** 2483-2485
- [225] Takeda N, Okabe Y, Kuwahara J, Kojima S and Ogisu T 2005 Development of smart composite structures with small-diameter fiber Bragg grating sensors for damage detection: Quantitative evaluation of delamination length in CFRP laminates using Lamb wave sensing *Composites Science and Technology* **65** 2575-2587
- [226] Taki M, Muanenda Y S, Toccafondo I, Signorini A, Nannipieri T and Di Pasquale F 2014 Optimized hybrid Raman/Fast-BOTDA sensor for temperature and strain measurements in large infrastructures *IEEE Sensors Journal* **14** 4297-4304
- [227] Tanaka N, Okabe Y and Takeda N 2003 Temperature-compensated strain measurement using fiber Bragg grating sensors embedded in composite laminates *Smart Materials and Structures* **12** 940-946
- [228] Teughels A and Roeck G D 2005 Damage detection and parameter identification by finite element model updating *Archives of Computational Methods in Engineering* **12** 123-164
- [229] Thostenson E T and Chou T W 2006 Carbon nanotube networks: sensing of distributed strain and damage for life prediction and self-healing *Advanced Materials* **18** 2837-2841
- [230] Tibaduiza Burgos D, Gomez Vargas R, Pedraza C, Agis D and Pozo F 2020 Damage identification in structural health monitoring: A brief review from its implementation to the use of data-driven applications *Sensors* **20** 733
- [231] Todd M D, Johnson G A and Vohra S T 2001 Deployment of a fiber Bragg grating-based measurement system in a structural health monitoring application *Smart Materials and Structures* **10**(3) 534-539
- [232] Ubertini F, D'Alessandro A, Downey A, Garca-Macas E, Laflamme S and Castro-Triguero R 2018 Recent advances on SHM of reinforced concrete and masonry structures enabled by self-sensing structural materials *Proceedings* **2**(3) 119
- [233] Udd E 1995 An overview of fiber-optic sensors *Review of Scientific Instruments* **66** 4015-4030
- [234] Udd E and Spillman Jr W B 2011 *Fiber Optic Sensors: An Introduction for Engineers and Scientists* 2nd edition, John Wiley & Sons: Hoboken, NJ, USA
- [235] Uttam D and Culshaw B 1985 Precision time domain reflectometry in optical fiber systems using a frequency modulated continuous wave ranging technique *Journal of Lightwave Technology* **3**(5) 971-977
- [236] Venkatesh S and Dolfi D W 1990 Incoherent frequency modulated cw optical reflectometry with centimeter resolution *Applied Optics* **29**(9) 1323-1326
- [237] Villalba S and Casas J R 2013 Application of optical fiber distributed sensing to health monitoring of concrete structures *Mechanical Systems and Signal Processing* **39**(1-2) 441-451
- [238] Vrgoc A, Tomicevic Z, Smaniotto B and Hild F 2021 Application of different imaging techniques for the characterization of damage in fiber reinforced polymer *Composites Part A Applied Science and Manufacturing* **150** 106576
- [239] Waeytens J, Rosic B, Charbonnel P-E, Merliot E, Siegert D, Chapeleau X, Vidal R, Le Corvec V and Cottineau L-M 2016 Model updating techniques for damage detection in concrete beam using optic fiber strain measurement device *Engineering Structures* **129** 2-10
- [240] Wang B, Fan X, Wang S, Yang G, Liu Q and He Z 2016 Laser phase noise compensation in long-range OFDR by using an optical fiber delay loop *Optics Communications* **365** 220-224

- [241] Wang C, Li Z, Gui X, Fu X, Wang F, Wang J and Bao X 2019 Micro-cavity array with high accuracy for fully distributed optical fiber sensing *Journal of Lightwave Technology* **37**(3) 927-932
- [242] Wang S, Lasn K, Westum Elverum C, Wan D and Echtermeyer A 2020 Novel in-situ residual strain measurements in additive manufacturing specimens by using the Optical Backscatter Reflectometry *Additive Manufacturing* **32** 101040
- [243] Wang Y, Lu P, Mihailov S, Chen L and Bao X 2020 Strain measurement range enhanced chirped pulse ϕ -OTDR for distributed static and dynamic strain measurement based on random fiber grating array *Optics Letters* **45**(21) 6110-6113
- [244] Weber B, Paultre P and Proulx J 2007 Structural damage detection using nonlinear parameter identification with Tikhonov regularization *Structural Control Health Monitoring* **14**(3) 406-427
- [245] Wheeler L N, Pannese E, Hoult N A, Take W A, Le H 2018 Transportation geotechnics measurement of distributed dynamic rail strains using a Rayleigh backscatter based fiber optic sensor: Lab and field evaluation *Transportation Geotechnics* **14** 70-80
- [246] Xie K, Rao Y and Ran Z 2008 Distributed optical fiber sensing system based of Rayleigh scattering light ϕ -OTDR using single-mode fiber laser with high power and narrow linewidth *Acta Optica Sinica* **28**(3) 569-572
- [247] Yang J N, Lin S, Huang H and Zhou L 2006 An adaptive extended Kalman filter for structural damage identification *Structural Control Health Monitoring* **13**(4) 849-867
- [248] Yang Z, Soto M A and Thévenaz L 2016 Increasing robustness of bipolar pulse coding in Brillouin distributed fiber sensors *Optics Express* **24** 586-597
- [249] Ye X W, Su Y H and Han J P 2014 Structural health monitoring of civil infrastructure using optical fiber sensing technology: A comprehensive review *Scientific World Journal* 652329
- [250] Young A T 1981 Rayleigh scattering *Applied Optics* **20**(4) 533-535
- [251] Yuan L, Liu Z, Yang J 2007 Rayleigh backscattering fiber optic rotation sensor based on combined two-ring-resonator. *Sensors and Actuators A - Physical* **136**(1) 216-220
- [252] Yuksel K, Wuilpart M and Mégret P 2009 Analysis and suppression of nonlinear frequency modulation in an optical frequency-domain reflectometer *Optics Express* **17** 5845-5851
- [253] Zadok A, Antman Y, Primerov N, Denisov A, Sancho J and Thevenaz L 2012 Random-access distributed fiber sensing *Laser & Photonics Reviews* **6** L1-L5
- [254] Zhang H, Bilotti E and Peijs T 2016 The use of carbon nanotubes for damage sensing and structural health monitoring *Nanocomposites* **1**(4) 167-184
- [255] Zhang Y, Meng F, Song Y, Dong M and Zhu L 2019 Characterization of metallic-packaging fiber Bragg grating sensors with coated and bare fibers *Applied Optics* **58**(6) 1426-1432
- [256] Zhao S, Cui J, Suo L, Wu Z, Zhou D and Tan J 2019 Performance investigation of OFDR sensing system with a wide strain measurement range *Journal of Lightwave Technology* **37**(15) 3721-3727
- [257] Zhao S, Cui J, Wu Z, Wang Z and Tan J 2021 Distributed fiber deformation measurement by high-accuracy phase detection in OFDR scheme *Journal of Lightwave Technology* **39**(12) 4101-4108
- [258] Zhou G and Sim L M 2002 Damage detection and assessment in fibre-reinforced composite structures with embedded fiber optic sensors – review *Smart Materials and Structures* **11** 925-939
- [259] Zhou D P 2013 Distributed temperature and strain discrimination with stimulated Brillouin scattering and Rayleigh backscatter in an optical fiber *Sensors* **13** 1836-1845
- [260] Zhou D P, Chen L and Bao X 2016 Distributed dynamic strain measurement using optical frequency-domain reflectometry *Applied Optics* **55**(24) 6735-6739
- [261] Zhu P, Feng X, Liu Z, Huang M, Xie H and Soto M A 2021 Reliable packaging of optical fiber Bragg grating sensors for carbon fiber composite wind turbine blades *Composites Science and Technology* **213** 108933
- [262] Zoboli M and Bassi P 1983 High spatial resolution OTDR attenuation measurements by a correlation technique *Applied Optics* **22**(23) 3680-3681